Shape memory performance of bio-based polyester blends 4D printed by Fused Granulate Fabrication (FGF)

Citation for the original published paper (version of record):
Ponkratenkova, A., Starkova, O., Beluns, S. et al (2026). Shape memory performance of bio-based polyester blends 4D printed by Fused Granulate
Fabrication (FGF). Materials Today Communications, 53.
http://dx.doi.org/10.1016/j.mtcomm.2026.115415

Materials Today Communications 53 (2026) 115415

Contents lists available at ScienceDirect

Materials Today Communications

journal homepage: www.elsevier.com/locate/mtcomm

Shape memory performance of bio-based polyester blends 4D printed by Fused Granulate Fabrication (FGF)

Alisa Ponkratenkova [a,*], Olesja Starkova [a], Sergejs Beluns [a], Oskars Platnieks [a], Anete Tropa [a], Toms Valdemars Eiduks [b], Roland Kádár [c], Sergejs Gaidukovs [a,d,**]

[a] Institute of Chemistry and Chemical Technology, Faculty of Natural Sciences and Technology, Riga Technical University, P. Valdena 3, Riga LV–1048, Latvia
[b] Institute of Materials and Surface Engineering, Faculty of Natural Sciences and Technology, Riga Technical University, P. Valdena 3, Riga LV-1048, Latvia
[c] Department of Mechanical Engineering, Chalmers University of Technology, Gothenburg 41296, Sweden
[d] Department of Materials Science and Engineering, Korea University, Seoul 02841, Republic of Korea

ARTICLE INFO

Keywords:
Screw Extrusion-Based 3D Printing
Poly(3-hydroxybutyrate)
Poly(lactic acid)
Poly(butylene succinate-*co*-butylene adipate)
Additive manufacturing
Thermoresponsive materials

ABSTRACT

With the rise of advanced manufacturing technologies such as Fused Granulate Fabrication (FGF), the influence of processing routes on the shape-memory behavior of bio-based polymers remains poorly understood. This study investigates poly(hydroxybutyrate) (PHB)/poly(lactic acid) (PLA)/poly(butylene succinate-*co*-adipate) (PBSA) biopolyester blends 3D-printed using FGF under varied programming conditions to establish structure–process–property relationships relevant to 4D printing. Comparing compression-molded and printed samples revealed how fabrication and printing-induced orientation affect morphology, mechanical properties, and the shape memory effect (SME) response. PLA75-PBSA25 demonstrated superior mechanical performance (strength ≈40.00 MPa, modulus ≈1.10 GPa) and SME efficiency, achieving nearly perfect shape fixity (R_f ≈ 100%) and high recovery (R_r ≈90.0%). Based on combined SME and mechanical performance, the blends can be ranked as: PLA75-PBSA25 > PHB25-PLA50-PBSA25 > PHB33-PLA33-PBSA33 > PHB50-PLA25-PBSA25 > PHB75-PBSA25. Programming temperature had a significant influence on SME: cold programming resulted in incomplete fixation, hot programming caused partial loss of recovery due to plastic deformation, while warm programming (60 °C) yielded the most balanced and repeatable performance. 3D-printed samples retained SME efficiency within 10.0% of that of compression-molded counterparts. Layers printed parallel to the deformation direction exhibited slightly higher recovery than those printed at 90°. Cyclic testing confirmed that PLA75-PBSA25 retained stable SME performance over 15 cycles, while other blends exhibited moderate fatigue. Overall, optimized phase compatibility and warm-programming conditions enabled the reliable synthesis of SME, identifying PLA75-PBSA25 as a promising material for durable 4D-printed shape memory applications.

1. Introduction

The emergence of 4D printing, which combines additive manufacturing and stimuli-responsive materials, has opened up new possibilities for creating structures that can change their shape or function when exposed to external triggers, such as heat [1,2], moisture [3–5], electric field [6], light [7], or magnetic field [8,9]. Among the various materials explored for 4D printing, shape memory polymers (SMPs) stand out because of their low density, large recoverable deformation, and adjustable thermal response [10,11]. Programmable materials enable control over shape transformations, and as a result, expand their use in soft robotics [12,13], biomedical devices [14–16], and adaptive structures [17–19]. Still, achieving predictable, repeatable shape-memory behavior in 3D-printed components remains challenging, as it depends on the complex interplay among material composition, processing parameters, and structural anisotropy [20–22].

Poly(lactic acid) (PLA) and poly(hydroxybutyrate) (PHB) are promising bio-based and biodegradable polymers with excellent biocompatibility and non-toxic degradation [23]. PLA exhibits a glass transition temperature (T_g) of 55–65 °C, enabling thermoresponsive switching at

* Corresponding author.
** Corresponding author at: Institute of Chemistry and Chemical Technology, Faculty of Natural Sciences and Technology, Riga Technical University, P. Valdena 3, Riga LV–1048, Latvia.
E-mail addresses: alisa.ponkratenkova@rtu.lv (A. Ponkratenkova), sergejs.gaidukovs@rtu.lv (S. Gaidukovs).

https://doi.org/10.1016/j.mtcomm.2026.115415
Received 2 March 2026; Received in revised form 18 May 2026; Accepted 20 May 2026
Available online 20 May 2026

moderate temperatures, whereas PHB shows a broader, system-dependent T_g (0–60 °C) and higher crystallinity, contributing to structural stability and shape fixation. Nevertheless, PHB melting temperature (170–180 °C) lies close to its degradation onset, resulting in a narrow processing window, which aligns with PLA melting range of 160–180 °C [23]. PLA and PHB both exhibit relatively high stiffness, with elastic moduli typically in the range of ~2–3 GPa for PLA and ~3–4 GPa for PHB, providing sufficient rigidity for structural support. These polymers enable the design of smart materials and 4D-printed systems, including shape-morphing structures, self-fitting orthopedic devices, and stimuli-responsive components. To overcome the inherent brittleness and limited deformability of PLA and PHB, poly(butylene succinate-*co*-adipate) (PBSA) can be introduced as a flexible system modifier to form binary blends, improve elongation at break, and facilitate the chain mobility required for reliable shape memory behavior and repeated actuation. PBSA aligns well with PLA and PHB, sharing key benefits, including bio-based, biocompatible, and compostable properties. To further advance shape memory materials, ternary blend combinations can be explored. PLA and PHB combination enables dual-transition behavior, where PLA governs the switching phase, and PHB contributes to fixation with higher crystallinity [23], supporting the design of 3D-printed smart systems. Yang et al. studied how molten PBSA droplets acted as nucleating agents for plasticized PLA [24]. Mathew et al. produced a bio-based filament from a PLA matrix containing varying amounts of poly(butylene adipate-*co*-terephthalate) (PBAT), a similar soft polyester to PBSA [25]. Increasing the PBAT concentration to 30 wt% notably improved the material's toughness and impact resistance. Kanabenja et al. demonstrated that 3D printed specimens from PHB and PLA with hydroxyapatite (HA) and poly(propylene glycol) (PPG) used as a reinforcing agent and plasticizer, exhibited excellent mechanical properties, which included impact strength of 1.85 kJ/m2, flexural modulus of 3.20 GPa, and flexural stress of 42.50 MPa [26]. Current 3D-printed shape-memory polymers are predominantly based on flexible systems such as polyurethanes or modified polyesters, which limit their mechanical stiffness and restrict their use in load-bearing applications [27–29]. Therefore, developing SMP blends that combine high-stiffness with reliable shape recovery remains a key challenge.

The shape memory effect (SME) in thermoplastic SMPs arises from two distinct phases: a rigid phase that defines the permanent shape and a reversible phase responsible for temporary deformation [30]. The T_g typically acts as the switching point, where deformation is fixed and later recovered through the release of stored internal stresses generated during programming [4,22,31–34]. Stress relaxation and the balance between elastic and plastic deformation depend on programming conditions such as temperature, strain, and fixation time [11,27,35]. These parameters strongly influence the resulting shape memory performance. Conventionally, SMPs are programmed above T_g (hot programming), where the material is deformed and then cooled to fix the temporary shape [30,36]. The width of the glass transition region (tan δ peak) also plays an important role, as broader transitions allow for more flexible and stable actuation, which is particularly relevant for 4D printing applications [10,37]. However, sub-T_g approaches (warm and cold programming) are gaining attention as more energy-efficient alternatives [38–40], where cold programming occurs below T_g and warm programming near T_g. These methods reduce thermal exposure and processing demands, minimizing irreversible structural changes and excessive plastic deformation [33], but are often associated with slower response due to reduced molecular mobility [39]. Therefore, selecting an optimal programming temperature remains critical to balance energy efficiency with reliable and repeatable shape memory performance. This study takes a step forward in this direction by evaluating SME at different sub-T_g programming conditions to identify temperature protocols that are both practical and effective for novel biopolyester-based SMPs.

Material extrusion 3D printing with polymer granules or pellets, known as Fused Granulate Fabrication (FGF), has gained increasing attention as an alternative to traditional filament-based printing [41]. Some of the existing research articles have already shown that it works well with thermoplastics, such as PLA [42,43], poly(ether ether ketone) [44], poly(ε-caprolactone) [45], acrylonitrile butadiene styrene [46], along with more complex systems like polymer blends [47], fibre-reinforced [48], and higliy loaded polymer composites [49]. FGF skips the filament-making step entirely and uses raw or directly compounded materials instead. This simplifies the entire processing chain, reduces costs, and helps avoid additional thermal degradation that often occurs during filament production [50,51]. In addition, FGF is much more flexible in its material design. It is easier to experiment with polymer blends, higher filler contents, or recycled materials, which is not always straightforward in filament-based printing [41,52].

On top of that, these systems usually allow much higher printing speeds and material throughput, which is why they are often considered for large-scale or industrial applications [41,46]. Still, issues like unstable material feeding, less consistent extrusion, weaker interlayer bonding, and lower dimensional accuracy can be problems compared to conventional filament printing [41,53]. Even so, the overall potential of FGF is quite significant, especially toward sustainable materials and circular manufacturing. The ability to directly process recycled, blended polymers or bio-based composites makes it a very relevant technology going forward [41]. Continued research is therefore important, particularly in optimizing material rheology, improving process control, and better understanding the structure–property relationships of polymer materials processed using the FGF technique. Based on the available literature, only one closely related study has been reported. Cersoli et al. explored the processing of a commercial polyurethane-based shape memory polymer using a pellet-based extrusion approach [54]. Nevertheless, this work is fundamentally different from that of Cersoli et al., both in the material system employed and in the underlying research objectives.

In our previous studies, we investigated the mechanical, thermal, structural, and rheological properties of neat polymer, polymer blends, and 3D-printed samples [55–57], as well as the durability of 3D-printed polymer blends [58]. Based on the previous results, we selected the most effective formulations. The primary objective of this study is to evaluate how the processing route (compression molding vs. FGF) influences the shape memory performance of PHB/PLA/PBSA blends. The effects of key programming parameters, including programming temperature, applied strain, and fixation time, on shape fixity, recovery ratio, and recovery stress are systematically assessed. Neat polymers (PHB, PLA, PBSA) and compression-molded samples were used as reference (control) systems to evaluate the effect of FGF processing on morphology, mechanical properties, and shape memory behavior. A direct comparison between conventional and additive processing provides insight into the extent to which FGF can approach the reliability and durability of established methods while minimizing system-related bias. These findings contribute to understanding the processing-structure-property-function relationships and support the development of sustainable, high-stiffness shape-memory systems for emerging 4D printing applications.

2. Materials and Methods

2.1. Materials

In this study, three different commercially available industrially produced biopolyesters were used. Poly(butylene succinate-*co*-butylene adipate) (PBSA) grade FD92PM was purchased from PTT MCC Biochem Co., Ltd. (Bangkok, Thailand). PBSA (BioPBS™ FD92PM) is a semi-crystalline polyester with a density of 1.24 g/cm^3 and an MFI of 4 g/10 min (190 °C, 2.16 kg). It is bio-based, biodegradable, and DIN CERTCO-certified (8C083). Poly(3-hydroxybutyrate) (PHB) grade ENMAT Y3000P is a semi-crystalline bio-based thermoplastic polyester

(1.25 g/cm^3, T_m 175–180 °C) with an MFI of 8–15 g/10 min (190 °C, 2.16 kg). Poly(lactic acid) (PLA) with trademark Ingeo™ and grade 6201D produced by NatureWorks LLC is 100% bio-based. It is characterized by a melting temperature of approximately 170 °C, an MFI of 15–30 g/10 min (210 °C, ASTM D1238), and a density of 1.24 g/cm^3.

2.2. Blend, sheets, and pellet preparation

Polymer granules were dried in a vacuum furnace (J.P. Selecta) at 60 °C (5–20 mbar) for 24 h before processing. The blends were prepared using a Brabender Mixer 50EHT (Germany) with a blending temperature of 185 °C and a rotation speed of 70 rpm. Premixed compositions (Table 1) were used.

A Carver CH 4386 hydraulic press (USA) was used to prepare sheets with thicknesses of 0.40 ± 0.02 and 2.00 ± 0.05 mm for testing purposes. Compression-molded sheets in wide bar shape (samples dimensions length (L) × width (W) × height (H) = 75 mm × 10 mm × 0.4 mm) for tensile testing, thin bar shape (L × W × H = 75 mm × 5 mm × 0.4 mm) for shape memory and dynamic mechanical testing, and disc (diameter (D) × H = 25 mm × 0.4 mm) for rheology. Sheets with a thickness of 2.00 mm were used for granule preparation. All samples were prepared under identical processing conditions, and their thicknesses were set by a selected mold and controlled with the thickness gauge. The mold temperature was set to 185 °C. The samples were first preheated for 2 min without pressure, compressed for 3 min under a 30 kN load, and cooled for 5 min between steel plates (30 kg weight) to ensure controlled cooling.

For pellet preparation, sheets were first immersed in liquid nitrogen to facilitate embrittlement, then ground into smaller pieces using a grinder to produce granules about 2 mm in size. The preparation of 2 mm sheets prior to pelletization was necessary to produce granules with consistent geometry suitable for FGF processing. Direct pelletization from the melt-mixed materials was not feasible due to the selected mixing method with the Brabender Mixer 50EHT.

2.3. Fused Granulate Fabrication (FGF)

The samples were printed using the FGF technique on a Tumaker NX Pro 3D printer. 3D-printed specimens used for testing were designed in SolidWorks according to the ISO 527–1B standard. Dumbbell-shaped specimens (L × W × H = 75 mm × 10 mm × 2 mm) for tensile testing and bar-shaped specimens (L × W × H = 75 mm × 5 mm × 0.4 mm) for shape-memory characterization were 3D printed with layers aligned to the deformation direction (0°) or perpendicular to it (90°) using a Simplify3D slicer (Fig. 1a). No brim was used during printing. In addition, sample images of the specimens produced by both 3D printing and compression molding are shown in Figure A.1. All samples were printed under the same conditions, which are summarized in Table 2. Printing was carried out via continuous material deposition without intentional pauses between layers. Also, no active cooling, such as a cooling with fan, was used during the process.

Table 1
Abbreviations and formulations.

Sample	PHB (B) (wt%)	PLA (L) (wt%)	PBSA (A) (wt%)
PHB	100.0	–	–
PLA	–	100.0	–
PBSA	–	–	100.0
B75-A25	75.0	–	25.0
L75-A25	–	75.0	25.0
B33-L33-A33*	33.3	33.3	33.3
B50-L25-A25	50.0	25.0	25.0
B25-L50-A25	25.0	50.0	25.0

* values normalized to 100 wt% and rounded to one decimal place.

2.4. Testing Methods

2.4.1. Scanning Electron Microscopy (SEM)

Scanning Electron Microscopy (SEM) was performed using a Hitachi Tabletop Microscope TM3000 (Japan). Fractured surfaces were prepared by immersing specimens in liquid nitrogen. In the next step, the etched surface was prepared by immersing the samples in acetone for 24 h at 20 °C, followed by an additional hour at 30 °C. No coatings were used for imaging. An acceleration voltage of 5 kV was used for image generation.

2.4.2. Rheology

An Anton Paar Smart-Pave 102 (Graz, Austria) was used to measure the rheology of the polymer melt. A 25 mm parallel-plate measuring geometry with a 0.4 mm gap and a system temperature held constant at 185 °C was used. Linear viscoelastic oscillatory shear measurements were performed at an angular frequency range of 0.1–628 rad/s and a fixed strain amplitude of 5%.

2.4.3. Dynamic mechanical thermal analysis (DMTA)

Dynamic mechanical thermal analysis (DMTA) was performed using a Mettler Toledo (USA) DMA/SDTA861e. A standard tension clamping assembly was used. The testing protocol entailed a temperature range of −60–140 °C, a heating rate of 3 °C min^{-1}, a temperature accuracy of ± 0.5 °C, and 5 N of applied force with an elongation of 10 μm at 1 Hz. The T_g in this study was determined from both the tan δ maximum and the loss modulus peak. The instrument's temperature accuracy is estimated at ± 0.5 °C, which defines the primary measurement uncertainty.

2.4.4. Differential scanning calorimetry (DSC)

Differential scanning calorimetry (DSC) measurements were conducted on the Mettler Toledo DSC-1 (Horsham, PA, USA) analyzer. The measurements were performed under a nitrogen atmosphere and consisted of heating, cooling, and a second heating in the temperature range of −50–200 °C. The heating and cooling rates were 10 °C/min, the temperature accuracy was ± 0.2 °C, and the sample mass was approximately 10 mg, with the precise value measured using an analytical balance with a resolution of 0.00001 g.

2.4.5. Tensile tests

Tensile tests were performed using a Tinius Olsen model 25ST (Horsham, PA, USA) universal testing machine equipped with a thermal chamber at a crosshead speed of 5 mm/min and a gauge length of 40 mm. Tests were performed at 20, 40, 60, and 80 °C for compression-molded wide bar samples and at 20 and 60 °C for 3D-printed dog-bone samples. The tests were performed in accordance with ISO 527–3 for sheet specimens and ISO 527–1 and ISO 527–2 for dog-bone specimens, respectively. Prior to testing, all samples were conditioned in a thermal chamber for 5 min to ensure temperature equilibrium. Three replicates were tested for each compression-molded sample, and five replicates were tested for each 3D-printed sample at each temperature. The elastic modulus was determined from the linear region of the stress–strain curve within a strain range of 0.2–0.5%.

2.4.6. Shape memory tests

The shape memory effect (SME) was studied using bar-shaped samples (L × W × H = 75 mm × 5 mm × 0.4 mm) for all three sample types: compression-molded and 3D-printed samples oriented at 0° and 90° (Fig. 1a). The basic tests were conducted at a programming temperature (T_p) of 60 °C. Additionally, the effect of temperature was studied at 40 °C and 80 °C. These temperatures were selected based on DSC and DMTA results, which identified an effective switching temperature range of approximately 40–80 °C around the glass transition region. Accordingly, 40, 60, and 80 °C represent conditions below, near, and above the transition region, respectively, corresponding to cold, warm, and hot programming conditions. Further details are provided in Section

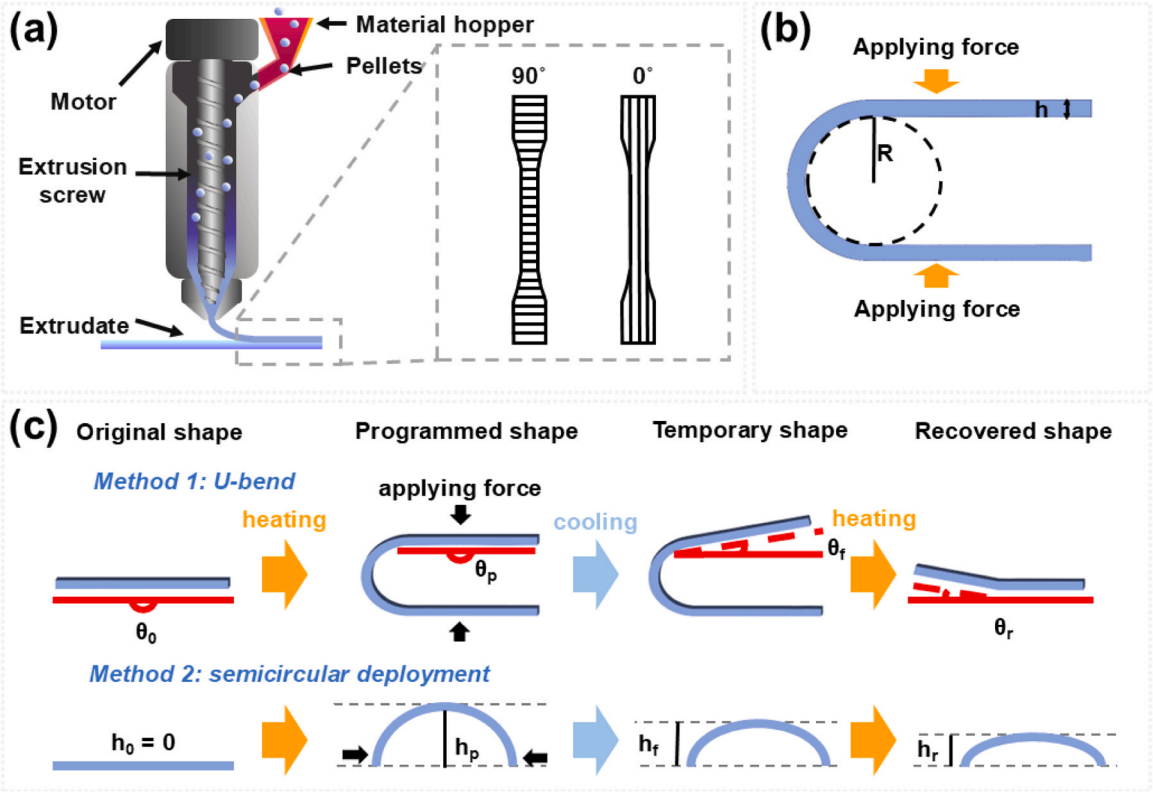

Fig. 1. (a) Sample preparation, (b) schematic illustration of the U-shaped bending test, (c) schematic illustration of shape memory tests according to Method 1 and Method 2.

Table 2
3D-printing parameters.

Parameters	0° 3D printed samples	90° 3D printed samples
Bed temperature	40 °C	40 °C
Printing temperature	185 °C	185 °C
Nozzle diameter	0.6 mm	0.6 mm
Extrusion speed	40 mm/min	40 mm/min
Infill type	concentric	rectilinear
Infill angle	0°	90°
Infill (%)	100%	100%
Chamber temperature	22 °C	22 °C
Layer thickness	0.2 mm	0.2 mm

3.4.

SME was evaluated using U-shaped deployment bending tests (Fig. 1b). A similar "folding-deploy" shape memory testing method has been employed in several studies [32,59–62]. This method provides a straightforward approach to determining the bending radius of flexible sheets around a round mold or a specified-diameter cylinder. The endurance of bending deformation can be qualitatively analyzed based on deployment behavior. The bending process is easy to perform manually, without complex equipment [63]. The bending endurance of a sheet depends on the material's thickness-to-radius ratio (Fig. 1b).

The bending strain (ε_{bend}) on the convex surface of a sheet deployed around a cylindrical object with radius R can be calculated using the following formula [63,64]:

$$\varepsilon_{bend} = \frac{h}{2R} \times 100 \quad (1)$$

where h is the sheet thickness and R is the bending radius of curvature (radius of the cylinder). If the bending strain surpasses the material-specific critical strain, a crack initiates on the outer surface of the curved region.

The shape memory tests were conducted in a heat-controlled water bath according to the following procedure: (I) the samples were heated for 60 s at the programming temperature; (II) while still heated, the samples were deformed into a U-shape with a load applied for a fixation time $t_f = 20$ s; (III) with the load still applied, the samples were rapidly cooled in an ice-water bath for 20 s to fix the temporary shape; (IV) the samples were then removed from the ice bath and placed at ambient conditions (20 °C), where a photograph was taken to monitor the fixed (temporary) shape; (V) the samples were reheated in the water bath at T_p for 20 s to induce shape recovery; (VI) finally, the samples were returned to ambient temperature, and a photograph was taken to monitor the recovered shape. Tests were performed on three replicate samples to confirm repeatability.

In this study, two methods were selected for the quantitative characterization of SME in the produced blend samples (Fig. 1c). These methods differ in the deployment radius (bending strain) and in the approach used to calculate the shape memory ratios. In the first method (Method 1: U-bend), the blend sheets were deployed over a glass cylinder with a radius of 8 mm, resulting in $\varepsilon_{bend} = 2.5\%$ (Eq. (1)). In the second method (Method 2: semicircular deployment), the sheets were bent over a glass cylinder with a radius 21.4 mm, resulting in $\varepsilon_{bend} = 0.9\%$.

In Method 1, the shape fixity ratio (R_f) and shape recovery ratio (R_r) were calculated based on the deployment angle, using the following formulas [60]:

$$R_f = \frac{\theta_p - \theta_f}{\theta_p - \theta_0} \times 100 \quad (2)$$

$$R_r = \frac{\theta_p - \theta_r}{\theta_p} \times 100 \quad (3)$$

where θ_0 is the initial angle in the original shape, θ_p is the programmed (maximal) angle, θ_f is the fixed angle after cooling in the

temporary shape, and θ_r is the recovered angle after reheating (Fig. 1c). Based on the test and sample conditions in this study, $\theta_0 = 0°$ and $\theta_p = 180°$. The deployment angles θ_f and θ_r were determined using the arctangent (arctan) based on the legs of a right triangle constructed from each photograph of the shaped samples.

In Method 2, R_f and R_r were calculated based on the height of the shaped samples, using the following formulas [65]:

$$R_f = \frac{h_p - h_f}{h_p - h_0} \times 100 \quad (4)$$

$$R_r = \frac{h_p - h_r}{h_p} \times 100 \quad (5)$$

where h_0 is the initial height in the original shape, h_p is the programmed (maximal) height, h_f is the fixed height after cooling in the temporary shape, and h_r is the recovered height after reheating (Fig. 1c). Based on the test and sample conditions in this study, $h_0 = 0$ and $h_p = 21.8$ mm, calculated for 75 mm-long sheets wrapped around a cylinder with a radius of 21.4 mm.

The effects of thermal cycling on the shape memory performance of the samples were evaluated over 15 repeated heating-cooling-heating cycles at $T_p = 60$ °C, with $t_f = 20$ s at each step. The tests were performed using Method 1 for both compression-molded and printed samples of L75-A25, B25-L50-A25, and B33-L33-A33. The remaining PHB-rich blends, B75-A25 and B50-L25-A25, were excluded from the study due to their poor shape memory performance and brittleness. R_f and R_r in each cycle, j were calculated according to Eqs. (6), and (7) [66–68]:

$$R_{fj} = \frac{\theta_p - \theta_{rj-1} - \theta_{fj}}{\theta_p - \theta_{rj-1} - \theta_0} \times 100, \quad j > 1 \quad (6)$$

$$R_{rj} = \frac{\theta_p - \theta_{rj}}{\theta_p} \times 100, \quad j > 1 \quad (7)$$

The effects of load fixation time were studied at $T_p = 40$ °C. L75-A25 compression-molded samples were selected for this investigation because they exhibited the most effective shape-memory performance. Tests were conducted at various fixation times t_f of 20 s, 1 min, 5 min, 10 min, and 30 min. The cooling time was equal to t_f, while the recovery time t_r was set to twice the fixation time ($t_r = 2\ t_f$) to allow sufficient stress relaxation, which occurs more slowly at lower temperatures. For each t_f, three cycles were performed. R_f and R_r were calculated using Eqs. (2)–(3) and Eqs. (6)–(7), respectively, for the repeated thermal cycles.

3. Results

3.1. Structural properties by SEM

The SEM micrographs (Fig. 2) provide qualitative insight into the phase morphology of the PHB-PLA-PBSA blends as a function of composition and processing. It should be noted that the images were obtained after selective phase dissolution; therefore, the observed features represent etched structures rather than the intact bulk morphology. As a result, the analysis is limited to qualitative interpretation and does not allow accurate determination of domain size or detailed interfacial characterization.

Across all compositions, the micrographs indicate the presence of droplet–matrix, lamellar, and partially co-continuous morphologies, depending on blend composition and phase compatibility. The binary B75-A25 blend exhibits a typical droplet–matrix structure, where the PBSA phase appears as dispersed domains within the PHB matrix (Fig. 2a). In contrast, the L75-A25 blend shows a more homogeneous and continuous morphology with lamellar features, suggesting improved phase interaction between PLA and PBSA (Fig. 2b). The ternary system B33-L33-A33 displays a mixed morphology, combining droplet-like domains with lamellar structures (Fig. 2c), indicating partial phase continuity alongside dispersed phases. For the ternary systems with asymmetric compositions, the PHB-rich blend (B50-L25-A25) exhibits a more heterogeneous structure with irregular and coarser features (Fig. 2d), whereas the PLA-rich blend (B25-L50-A25) appears comparatively finer and more uniform, with smaller dispersed features and a more pronounced co-continuous character (Fig. 2e).

A qualitative comparison between 0°- and 90°-printed samples and compression-molded sheets indicates broadly similar morphological features for a given composition. However, because no strictly matched side-by-side imaging analysis was performed, subtle processing-induced differences cannot be excluded. Therefore, the present SEM observations suggest that compositional effects are prominent, while the influence of processing should be interpreted with caution and regarded as qualitative rather than definitive. Overall, ternary blends exhibit increased morphological complexity compared to binary systems, reflected in rougher and more heterogeneous etched surfaces, which is consistent with previous reports [55,57].

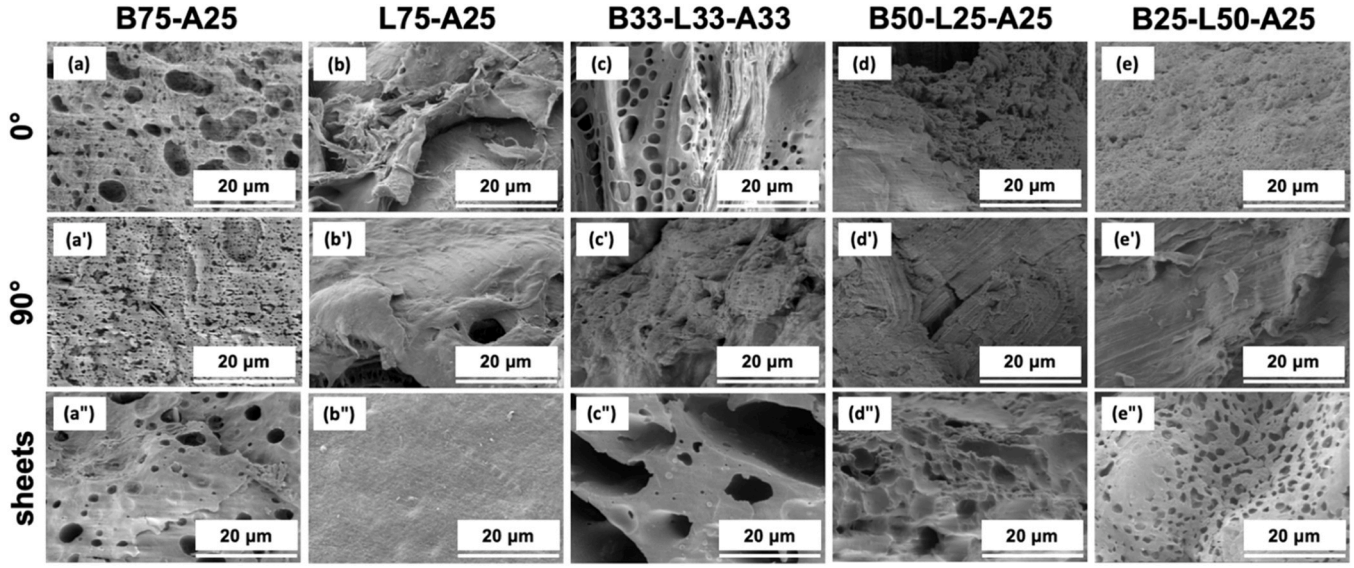

Fig. 2. SEM cross-section fracture surface of the (a) B75-A25, (b) L75-A25, (c) B33-L33-A33, (d) B50-L25-A50, (e) B25-L50-A25 blends from 0° (without quotation mark), 90° (single quotation mark), and sheets (double quotation mark) samples.

3.2. Rheology

The rheological properties of both neat polymers and blends are crucial for optimizing extrusion-based additive manufacturing processes [69,70]. Furthermore, rheological behavior determines how stress is stored and relaxed in the material, which directly affects shape memory programming and recovery. Fig. 3a and 3 b present the storage modulus (G′) and loss modulus (G″) as functions of angular frequency. Blends with finer morphologies and smaller characteristic domain sizes, such as L75-A25 (binary) and B33-L33-A33 (ternary), exhibit comparatively higher storage modulus values (Fig. 2, Fig. 3a and b), consistent with enhanced interfacial interactions and more efficient stress transfer between phases. Neat PHB and PBSA exhibit a crossover between G′ and G″ ($\tau = 1/\omega$), indicating a transition from viscous-dominated behavior at low frequencies to a more elastic melt response at higher frequencies, which reflects the presence of longer relaxation modes [71,72]. In contrast, neat PLA and all PHB-PLA-PBSA blends show G″ > G′ over the entire experimentally accessible frequency range, indicating predominantly viscous melt behavior with a limited contribution from long relaxation modes.

The complex viscosity function $|\eta^*|$ as a function of angular frequency, is shown in Fig. 3c and 3 d. All blends exhibit shear-thinning behavior, which facilitates stable extrusion through the nozzle at high shear rates while maintaining sufficient viscosity at lower shear rates to preserve shape fidelity after deposition. PLA-rich and ternary blends display viscosity levels comparable to neat PLA, whereas B75-A25 exhibits the lowest viscosity among the investigated compositions. As reported in the literature, neat PHB degrades over time at temperatures near or above its melting temperature, demonstrating a drop in viscosity at lower frequencies [73–75].

The complex viscosity functions were fitted using the Carreau-Yasuda model [76–78]:

$$|\eta^*| = |\eta_0^*|(1 + \lambda\omega^a)^{\frac{n-1}{a}} \quad (8)$$

where $|\eta^*|$ and $|\eta_0^*|$ are the complex viscosity and zero-shear complex viscosity magnitudes, respectively, λ is the relaxation time, a is a dimensional parameter, and n corresponds to the power-law index. A summary of the calculated rheological parameters is presented in Table A.1.

Of particular importance is the characteristic relaxation time λ, which spans nearly two orders of magnitude across the investigated materials. Neat PBSA exhibits the longest relaxation time (λ ≈ 0.100 s), whereas L75-A25 shows a markedly shorter relaxation time (λ ≈ 0.002 s), accompanied by pronounced shear-thinning behavior (n ≈ 0.25). The intermediate relaxation times observed for ternary blends (λ ≈ 0.016–0.029 s) reflect a balance between viscous flow and elastic response, which is consistent with their moderate shape-memory performance discussed in subsequent sections.

Overall, these rheological trends demonstrate that blending PHB, PLA, and PBSA enables tuning of melt behavior between more elastic, relaxation-dominated systems (PBSA-rich) and highly flowable, rapidly relaxing systems (PLA-rich), thereby optimizing the materials for fused granule fabrication while establishing relaxation timescales favorable for efficient shape memory programming and recovery [79,80].

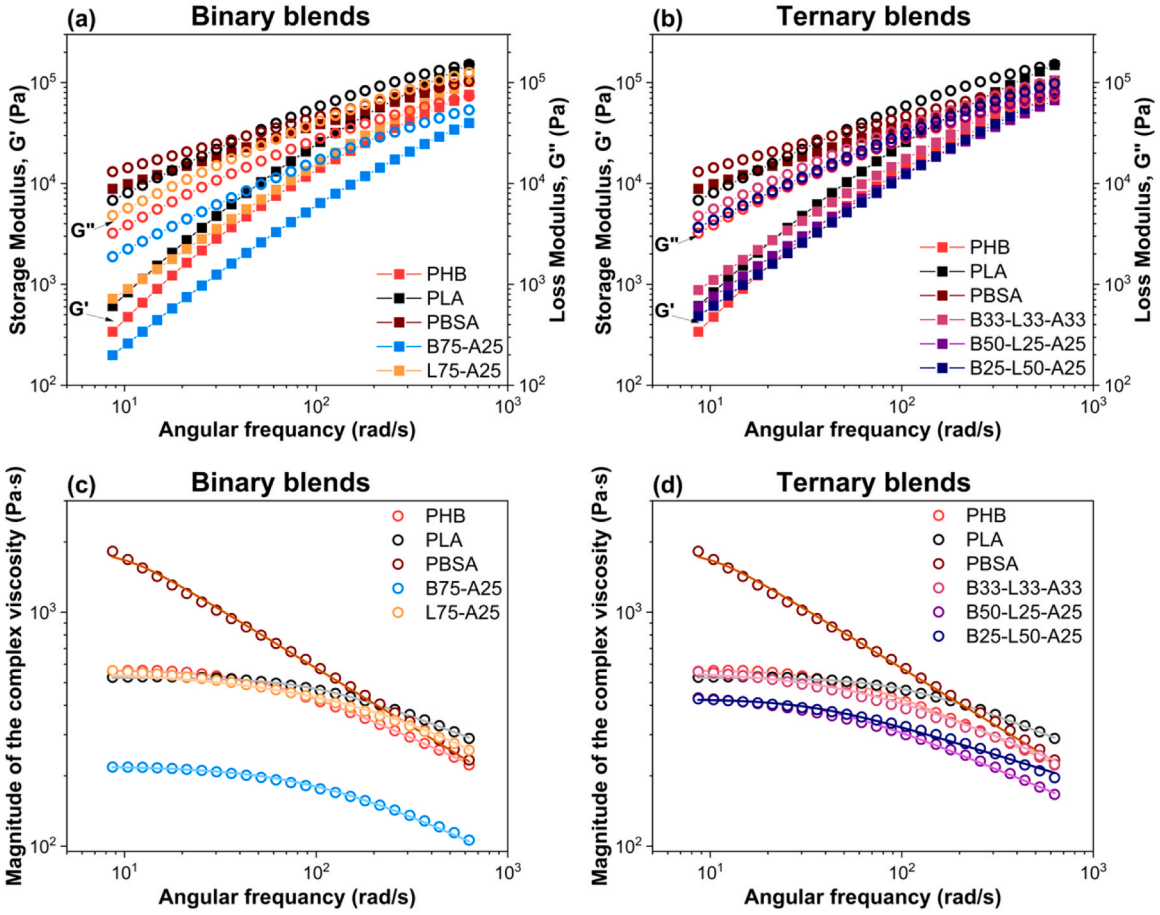

Fig. 3. (a, b) Storage modulus (G′) (filled symbols), loss modulus (G″) (empty symbols), and (c, d) the magnitude of the complex viscosity (|η*|) as a function of angular frequency (ω) for neat PHB, PLA, PBSA polymers, their binary and ternary blends.

3.3. Dynamic Mechanical Thermal Analysis

DMTA was performed to evaluate the thermomechanical transitions and viscoelastic behavior of the neat polymers and their blends. The temperature dependence of the storage modulus E′, loss modulus E″, and damping factor tan δ is shown in Fig. 4a–c, while the corresponding T_g determined from E″ and tan δ peaks are summarized in Table 3. The curves of E′, E″, and tan δ for the neat polymers are provided in Fig. A.2.

At sub-ambient temperatures, all materials exhibit high E′ values characteristic of the glassy state. PLA-based blends, except B33-L33-A33, maintain elevated E′ values over a broader temperature range, indicating improved structural integrity and efficient load transfer between phases. Thus, the addition of PLA to blends increased the blend's crystallinity, helping to attain superior storage modulus values up to the PLA's glass transition temperature. In contrast, PHB exhibits broader, lower-temperature relaxation features, reflecting increased heterogeneity in segmental mobility due to constraints imposed by its semi-crystalline morphology. As the temperature increases, the E′ of all blends gradually decreases, reflecting an increase in polymer chain mobility. A steep decline is observed in PLA-containing blends between 52.2 and 67.6 °C, corresponding to the glass transition temperature of PLA (Table 3). The E″ curves (Fig. 4b) show one or more peaks that represent different molecular motions in the material attributed to the glass transition. Neat PLA and PHB show single E″ maxima at 60.6 °C and 21.0 °C, respectively, while PBSA exhibits a transition near −23.7 °C. Commonly, polymer blends that display combined or shifted transitions, confirming the coexistence of different separate phases [34,81]. For example, B75-A25 shows two distinct relaxations (−31.5 °C and 12.5 °C), consistent with PBSA- and PHB-related segmental motions. Similarly, L75-A25 exhibits two peaks at −25.8 °C and 59.1 °C, corresponding to the PBSA and PLA domains, respectively. Ternary compositions such as B33-L33-A33 and B50-L25-A25 reveal three overlapping relaxations (−36.7 °C; 18.1–18.5 °C; 52.2–56.2 °C). The presence of multiple transitions, rather than a single, composition-dependent T_g, supports previous observations in rheology, namely the limited miscibility and phase-separated morphologies observed in the SEM images (Fig. 2), where droplet–matrix and co-continuous structures were evident, depending on composition.

The tan δ curves (Fig. 4c) further confirm these findings. Neat PLA exhibits a sharp peak at 67.2 °C, while PHB and PBSA show lower-

Table 3
Glass transition determined from tan δ and loss modulus E" peaks.

Sample	Polymer	tan δ peak(s), T_g (°C)	E" peak(s), T_g (°C)
PHB		24.7	21.0
PLA		67.2	60.6
PBSA		-16.5	-23.7
B75-A25	PHB	17.9	12.5
	PBSA	-26.3	-31.5
L75-A25	PLA	67.6	59.1
	PBSA	-22.1	-25.8
B33-L33-A33	PHB	20.8	18.1
	PLA	55.2	52.2
	PBSA	-33.7	-36.7
B50-L25-A25	PHB	24.8	18.5
	PLA	59.0	56.2
	PBSA	-34.7	-36.7
B25-L50-A25	PHB	n/d	n/d
	PLA	63.5	55.2
	PBSA	-21.4	-24.7

n/d – not detectable

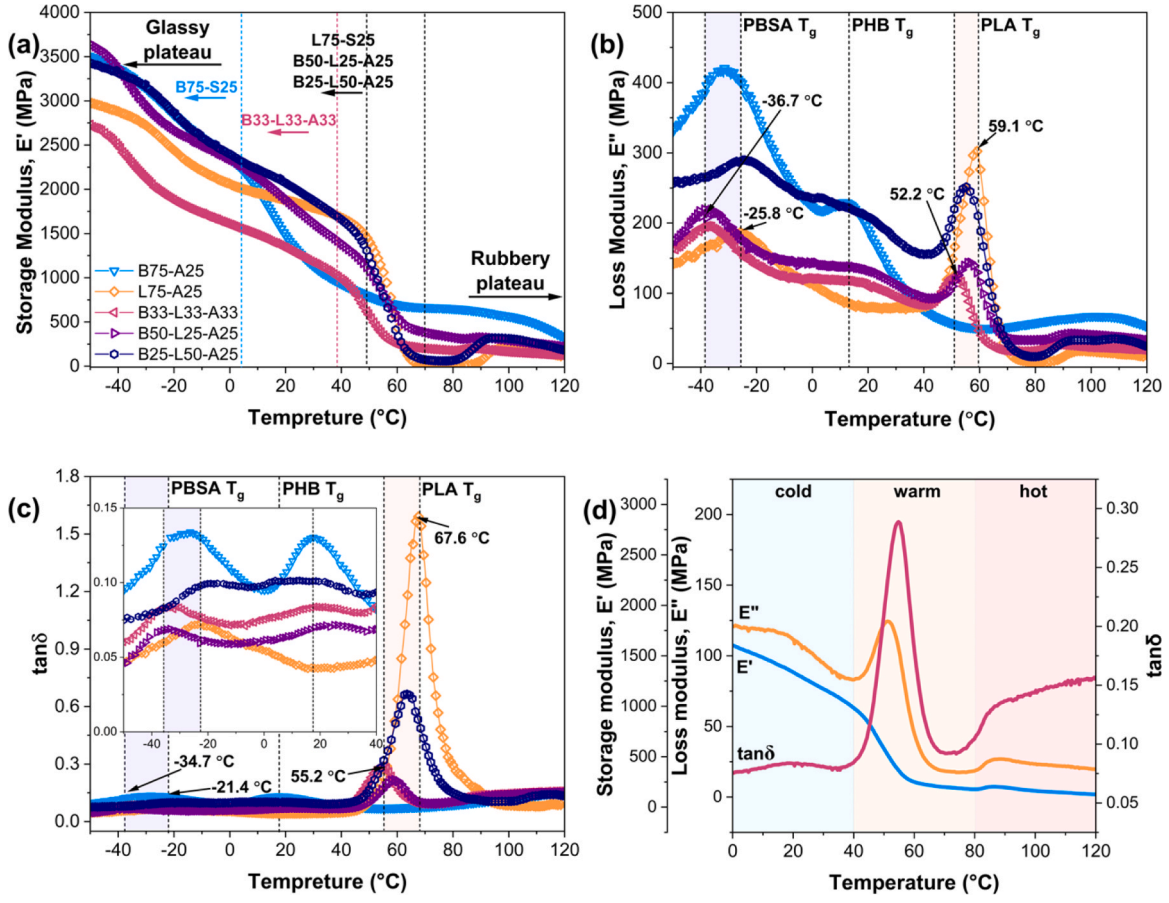

Fig. 4. (a) Storage modulus (E′), (b) loss modulus (E″), (c) tan δ as functions of temperature for PHB, PLA, PBSA binary and ternary blends. (d) Representative temperature dependences of E' (blue curve), E″ (orange curve), and tan δ (pink curve) for B33-L33-A33 blend.

temperature transitions at 24.7 °C and −16.5 °C, respectively. In the blends, the tan δ peaks shift with composition, reflecting interfacial interactions and phase distribution. For example, the B25-L50-A25 blend shows a dominant relaxation at 63.5 °C and a minor feature near −21.4 °C, indicating that PLA forms the continuous phase (Fig. 4e). The lower damping peak in PLA-rich blends reflects reduced segmental motion and enhanced interfacial adhesion, suggesting that amorphous chains are more constrained by interphase regions, leading to a more elastic and less dissipative response. This behavior aligns with the rheological and morphological observations discussed above, confirming that the thermal, viscoelastic, and structural characteristics are closely interrelated and collectively govern the printability, phase stability, and overall mechanical performance of the bio-based polymer blends.

The T_g is traditionally regarded as a critical design parameter for SMP programming; however, its value can vary significantly depending on the characterization method used. Data on the T_g values of the produced blends, determined from tan δ and loss modulus peaks, are compared in Table 3. According to tan δ data, the highest T_g (67.6 °C) was observed for the L75-A25 blend, while the lowest T_g (55.2 °C) was recorded for the B33-L33-A33 blend. The T_g values for other blends fall between these two values. In all cases, the T_g values determined from the loss modulus peak were found to be 2.0–9.0 °C lower than those obtained from the tan δ peaks. The L75-A25 blend also exhibited the broadest glass transition region, with a ΔT_g of 67.6 °C, followed by the B25-L50-A25 blend, which showed a slightly narrower ΔT_g of 63.5 °C. ΔTg was calculated as the temperature difference between the onset and endset of the tan δ peak. The onset and endset temperatures were defined based on the inflection points on the rising and descending sides of the tan δ peak, respectively. The uncertainty associated with this determination is estimated to be ± 4.0 °C. A broad glass transition region offers greater flexibility in selecting programming temperatures for shape memory behavior, thereby enhancing adaptability across various applications [37].

3.4. Differential Scanning Calorimetry (DSC)

DSC was performed to compare the thermal behavior of compression-molded and 3D-printed samples and to assess their "as-produced" thermal properties. Fig. 5 shows the first-heating scans, where all characteristic thermal transitions are evident, including the melting temperature (T_m), PLA glass transition temperature (T_g), and PLA cold crystallization temperature (T_{cc}). Thermal parameters extracted from the first-heating curves for both processing routes are summarized in Table 4.

Both binary and ternary blends consistently exhibited melting transitions attributable to their respective constituents. The heating scans showed prominent melting events at 169.6–175.4 °C, corresponding to PHB and PLA. As expected, ternary systems displayed overlap of these melting peaks, likely due to similar macromolecular interactions of PHAs and PLA [82].

Table 4
Calorimetric properties of compression-molded and 3D printed samples of PHB, PLA, PBSA binary and ternary blends.

Sample	Polymer	Compression-molded			3D printed		
		T_m (°C)	T_g (°C)	T_{cc} (°C)	T_m (°C)	T_g (°C)	T_{cc} (°C)
B75-A25	PHB	173.5	n/a	n/a	174.4	n/a	n/a
	PBSA	86.6	n/a	n/a	87.2; 112.9	n/a	n/a
L75-A25	PLA	171.8	60.6	91.7	170.6	60.5	86.4
	PBSA	84.3	n/a	n/a	114.6	n/a	n/a
B33-L33-A33	PHB	173.8	n/a	n/a	173.0	n/a	n/a
	PLA	173.8	60.6	96.7	173.0	59.5	93.6
	PBSA	86.7	n/a	n/a	87.2	n/a	n/a
B50-L25-A25	PHB	171.0	n/a	n/a	175.3	n/a	n/a
	PLA	171.0	59.6	93.8	175.3	58.9	94.8
	PBSA	85.4	n/a	n/a	87.1	n/a	n/a
B25-L50-A25	PHB	172.1	n/a	n/a	169.6	n/a	n/a
	PLA	172.1	58.6	95.4	169.6	60.2	92.0
	PBSA	86.4	n/a	n/a	111.9	n/a	n/a

n/a – not applicable

PBSA demonstrated more complex melting behavior. Although the manufacturer reports a PBSA melting point of approximately 84 °C [83], the blends exhibited PBSA-related melting peaks in two distinct regions: 84.3–87.2 °C and 111.9–114.6 °C. The multiple PBSA melting peaks indicate melting–recrystallization behavior during heating. The lower melting temperature corresponds to the melting of the less stable crystals. In contrast, the peak at a higher temperature was attributed to the melting of more stable crystals that form during heating [84–86].

Lower PBSA T_m values indicate restricted PBSA crystallization within the PLA/PHB-rich matrix. Restricted chain mobility and impeded lamellar growth lead to thinner, less perfect crystals, consistent with Gibbs–Thomson predictions [56,87]. While blends showing an upward shift in PBSA T_m indicate partial enhancement of PBSA crystal development, suggesting the formation of more stable and thicker lamellae. The effect was more pronounced in 3D-printed samples, consistent with slower cooling and enhanced crystal development.

Cooling curve (Fig. A.3 and corresponding data (Table A.2)) reveals two crystallization peaks for all binary and ternary blends, except for the L75-A25 3D printed sample. The presence of PBSA promoted crystallization of PLA, resulting in crystallinity of 13.0%. PHB exhibited a crystallization peak in the range of approximately 111.0–119.0 °C and

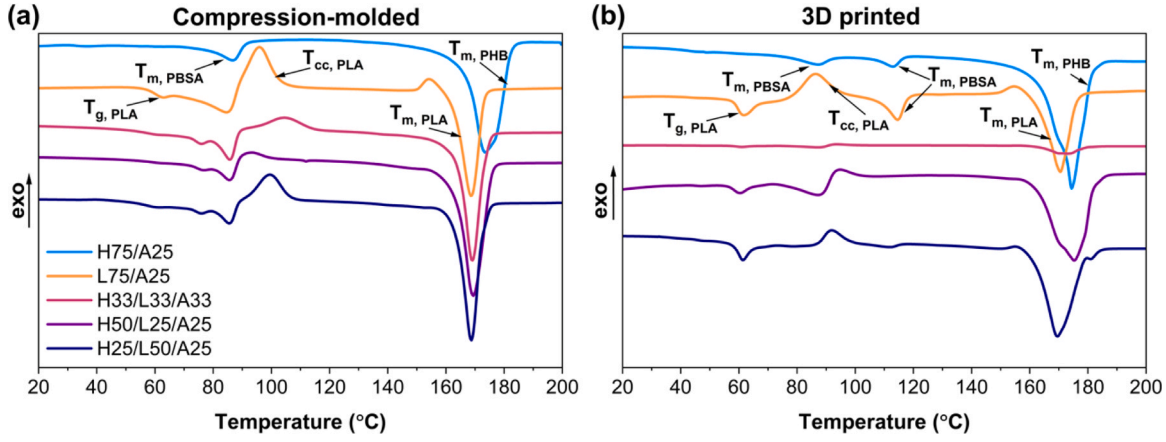

Fig. 5. First-heating DSC thermograms of (a) compression-molded sheets and (b) 3D-printed samples for binary and ternary PHB-PLA-PBSA blends.

was characterized by higher crystallinity (χ) values varying between 42.6% and 60.1%. In contrast, PBSA crystallization peak shows at lower temperatures, around 46.8–59.1 °C, with χ values in the range of approximately 16.1–22.7%.

PLA's T_g is typically observed near 60 °C [88]. In both compression-molded and 3D-printed samples, the T_g remained consistent (58.6–60.5 °C), indicating that the processing method does not significantly alter the segmental mobility of PLA. PLA commonly exhibits a T_{cc} during heating [89]. The lower T_{cc} of the 3D-printed samples suggests enhanced heterogeneous nucleation of PLA by PHB and PBSA domains. Additionally, both PHB and PBSA are known to accelerate PLA crystallization, acting as nucleating agents [90,91].

3.5. Mechanical properties

The stress–strain curves of 0°-printed samples tested at 20 and 60 °C are presented in Fig. 6, while 90°-printed samples showed comparable deformation behavior. The temperature dependencies of the tensile behavior of the compression-molded blends are shown in Fig. A.4. At 20 °C, all samples exhibited high stiffness (1.09–1.54 ± 0.03–0.19 GPa) and tensile strength (21.93–31.06 ± 1.28–6.16 MPa), characteristic of deformation in the glassy state. At 60 °C, all blends exhibited a pronounced reduction in modulus (0.56 ± 0.06 GPa to 0.12 ± 0.02 GPa) and strength (17.80 ± 1.13 MPa to 7.34 ± 0.39 MPa), marking the transition to a rubbery state with enhanced chain mobility but reduced load-bearing capacity. B75-A25 retained the highest modulus and strength at this temperature but remained brittle, whereas the PLA-rich blends showed the most pronounced softening, with a significantly increased strain at break. Differences between 0°- and 90°-printed samples were relatively small and did not show a consistent trend in tensile behavior.

These mechanical trends closely correlate with the observed morphological features (Fig. 2). Blends with finer, co-continuous morphologies, particularly those with a PLA-rich composition, exhibit enhanced ductility and greater strain at break, attributed to improved phase continuity and stronger interfacial adhesion between the components. In contrast, the droplet–matrix morphology of B75-A25 blend remained brittle and showed limited elongation. The presence of irregular, large droplet domains in PHB-rich blends further indicates lower mechanical uniformity and reduced strength. Elevated temperatures intensified these effects, highlighting the critical role of phase heterogeneity and morphological complexity in determining the overall mechanical response. Moreover, 3D-printed blends exhibited higher stiffness and strength (Fig. A.4). This suggests that printing-induced flow alignment, together with partial phase redistribution and orientation, contributes to improved load transfer and localized reinforcement along the extrusion path [10,55,67]. Overall, the correlation between morphology and mechanical response confirms that phase continuity and interfacial compatibility are key factors governing the deformation behavior of both compression-molded and 3D printed blends.

3.6. Shape memory properties

Shape fixity in SMP depends primarily on three factors [33,40,92]: (i) the programming temperature (T_p), (ii) the programming strain (ε_p), and (iii) the fixation time (t_f), i.e., the time allowed for stress relaxation.

Based on the DMTA results and the glass transition range of the blends, three representative programming temperatures were selected:

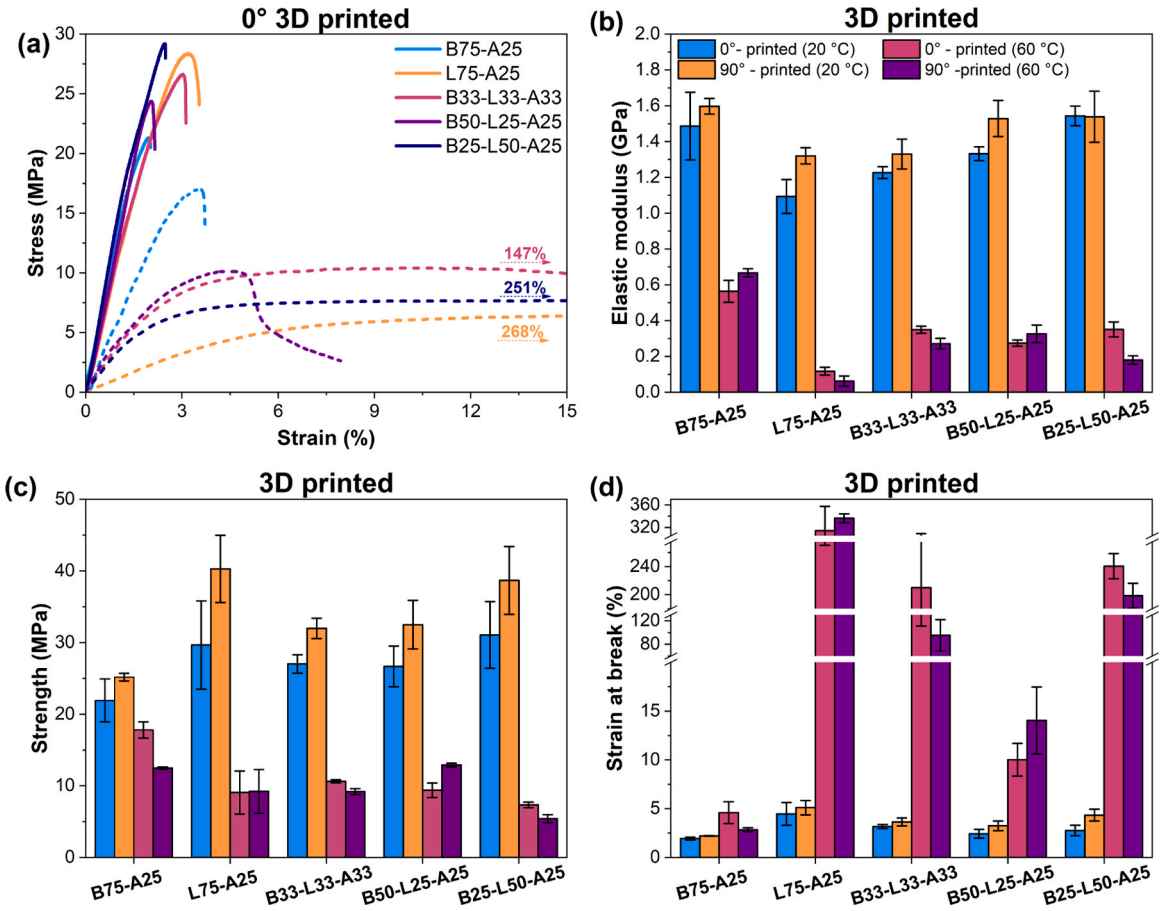

Fig. 6. Tensile test data for 3D printed samples: (a) representative stress-strain curves for 0°-printed samples at 20 °C (solid lines) and 60 °C (dashed lines); (b) elastic modulus; (c) strength; and (d) strain at break for 0°- and 90°-printed samples.

40 °C (cold), 60 °C (warm), and 80 °C (hot) (Fig. 4d). These correspond to the glassy region, the glass transition region, and the rubbery state, respectively, which are known to strongly influence molecular mobility and SME behavior [33,38,40].

3.6.1. *Effect of programming strain*

The effect of programming strain was investigated using two bending configurations with different radii. Method 1 ("U-bend") corresponds to a higher strain, where samples were bent over a glass cylinder with an outer radius of 8 mm, resulting in an inner bending strain of $\varepsilon_p = 1.88\%$. Method 2 ("semicircle") applies a lower strain, where a glass cylinder with an outer radius of 21.4 mm was used, corresponding to $\varepsilon_p = 0.70\%$ (see Section 2.4.6, Fig. 1b). Representative photographs of the samples in their temporary and recovered shapes for both methods are shown in Fig. 7.

The calculated SME coefficients, as shape fixity (R_f) and recovery (R_r) ratios of the blends, obtained by both methods, are summarized in Table 5. Both methods yielded comparable and repeatable results, with R_f and R_r values generally falling within the experimental scatter and exhibiting similar trends across blends. Method 2, however, exhibited greater variability than Method 1. Method 1 could not be applied to B75-A25 due to sample breakage at the higher bending strain.

Overall, programming strain within the studied range did not significantly affect R_f and R_r values, except for B75-A25. For L75-A25, R_f was consistently 100% in both methods, while R_r decreased from 89.0 ± 4.5% (Method 1) to 77.5 ± 14.8% (Method 2). B50-L25-A25 showed moderate fixity (74.7 ± 4.5% – 85.0 ± 11.8%) but the highest recovery values, remaining close to 90.0% in both cases. B25-L50-A25 achieved excellent fixity (>98.0%) but somewhat lower recovery (84.7 ± 7.1% – 85.0 ± 7.0%). B33-L33-A33 demonstrated balanced performance, with R_f of 90.5 ± 2.5% – 93.3 ± 6.7% and R_r of 85.0 ± 7.5% – 88.3 ± 3.2%. In contrast, B75-A25 in Method 2 exhibited the lowest R_f (39.5 ± 16.3%), while still maintaining a high recovery rate (88.5 ± 4.9%).

Overall, 3D printing did not significantly affect the shape memory performance of PLA-rich blends. For B50-L25-A25 and B33-L33-A33, the printed samples exhibited slightly reduced fixity and recovery compared to compression-molded sheets, yet still maintained reasonable shape memory functionality. In contrast, B75-A25 displayed the weakest SME response. R_r values obtained by Method 2 were lower than those from Method 1, despite the expectation that a lower programming strain would favor recovery. Since the same tendency was also observed for compression-molded samples, this discrepancy likely reflects methodological differences rather than intrinsic material properties.

Considering both fixity and recovery performance, the overall shape memory efficiency of the blends can be ranked as: L75-A25 > B25-L50-A25 > B33-L33-A33 > B50-L25-A25 > B75-A25. This sequence aligns well with blend mechanical behavior (Fig. 6, Fig. A.4). The L75-A25 blend, which exhibited the highest tensile strength, also showed the most pronounced SME response. The intermediate compositions (B25-L50-A25, B33-L33-A33, and B50-L25-A25) demonstrated balanced performance, emphasizing that the mechanical integrity and phase morphology of the blends closely govern SME behavior. Blends with more continuous or finely dispersed morphologies (Fig. 2), such as L75-A25 and B25-L50-A25, exhibited better interfacial adhesion and phase compatibility, enabling efficient stress transfer and elastic recovery during the SME cycle. Their co-continuous structures promote reversible

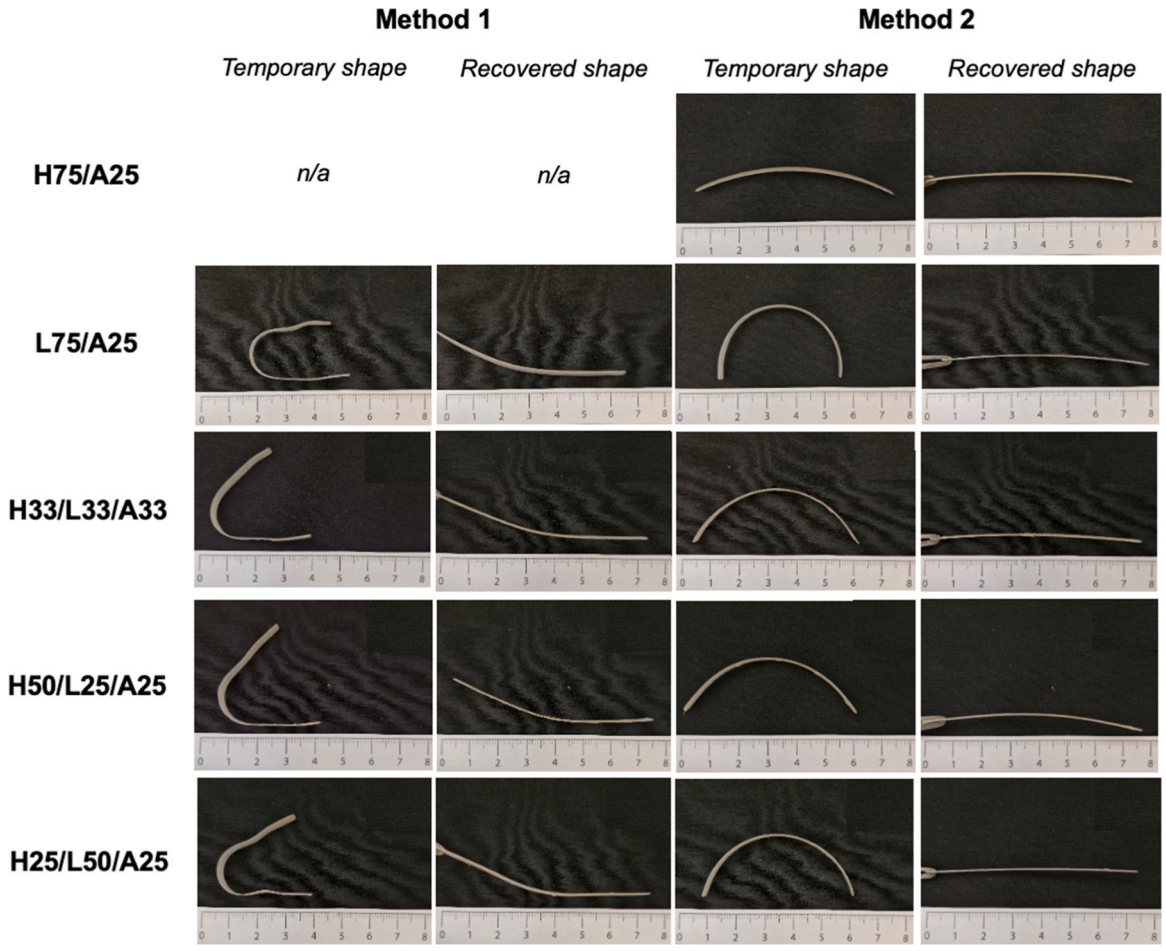

Fig. 7. Representative photographs of shape memory performance of 0°-printed samples in U-bend (Method 1) and semicircle deployment (Method 2) tests, $T_p = 60$ °C, $t_f = 20$ s.

Table 5
Fixity and recovery ratios of compression-molded and 3D printed samples, T_p = 60 ºC, t_f = 20 s.

Sample/orientation		Method 1 "U-bend" Compression-molded		ε_p = 1.88% 3D printed		Method 2 "Semicircle" Compression-molded		ε_p = 0.70% 3D printed	
		R_f (%)	R_r (%)	R_f (%)	R_r (%)	R_f (%)	R_r (%)	R_f (%)	R_r (%)
B75-A25	0°	n/a	n/a	n/a	n/a	39.5 ± 16.3	88.5 ± 4.9	54.5 ± 13.4	73.5 ± 2.1
	90°			n/a	n/a			61.5 ± 6.4	69.5 ± 3.5
L75-A25	0°	100.0 ± 0.0	89.0 ± 4.5	100.0 ± 0.0	79.5 ± 7.8	100.0 ± 0.0	77.5 ± 14.8	100.0 ± 0.0	85.5 ± 4.9
	90°			100.0 ± 0.0	84.5 ± 6.4			100.0 ± 0.0	87.5 ± 3.5
B33-L33-A33	0°	90.5 ± 2.5	85.0 ± 7.5	76.5 ± 0.7	90.3 ± 0.4	93.3 ± 6.7	88.3 ± 3.2	88.0 ± 2.8	84.5 ± 2.1
	90°			83.5 ± 2.1	84.3 ± 8.8			95.0 ± 2.8	86.0 ± 1.4
B50-L25-A25	0°	74.7 ± 4.6	91.7 ± 4.0	69.5 ± 2.1	89.0 ± 1.4	85.0 ± 11.8	89.8 ± 9.1	87.5 ± 2.1	79.5 ± 0.7
	90°			73.5 ± 0.7	89.0 ± 1.4			86.0 ± 2.8	91.5 ± 0.7
B25-L50-A25	0°	98.7 ± 1.3	84.7 ± 7.1	83.7 ± 1.5	88.0 ± 1.0	98.3 ± 1.7	85.0 ± 7.0	98.6 ± 1.4	86.0 ± 5.7
	90°			94.0 ± 2.8	86.5 ± 0.7			100.0 ± 0.0	85.5 ± 6.4

chain rearrangement, enhancing both fixation and recovery. Conversely, blends with droplet–matrix morphologies, particularly B75-A25, showed poor interfacial contact and localized stress accumulation, limiting deformation reversibility and leading to early fracture during programming [93]. These observations confirm that shape memory functionality in PHB-PLA-PBSA systems is morphology-controlled: finer, interconnected phases facilitate strain storage and recovery. Thus, optimizing blend composition and phase uniformity is crucial to achieving reliable and repeatable SME behavior in both compression-molded and 3D-printed systems.

3.6.2. *Effect of programming temperature*

Temperature dependences of R_f and R_r of the blends determined by Method 2 with t_f = 20 s are presented in Fig. 8. Similar dependences were also obtained by Method 1. Shape fixity R_f increased with programming temperature, showing the most substantial improvement between 40 °C and 60 °C, which corresponds to the onset of the glass-rubbery transition (see Table 3). At 80 °C, nearly perfect fixation (R_f ≈ 100%) with good repeatability was achieved for all blends except B75-A25, which fractured during bending. At 40 °C, R_f was much lower, remaining below 50.0% for most blends.

In contrast, R_r showed no explicit temperature dependence and remained relatively stable at 80.0–90.0% across all blends, though with greater scatter than R_f. Among the systems, L75-A25 demonstrated the best SME, combining excellent fixation (R_f = 100% at 60–80 °C) with high recovery (R_r ≈ 85.0–90.0%), indicating robust shape programming and reliable recovery. Despite differences in fixation ability, recovery ratios across blends were similar, and no delayed recovery effects were observed. The recovered shapes remained stable for several days under ambient conditions. No further quantitative assessments were conducted during the post-observation period.

Fig. 8c and d illustrate the effect of printing orientation on the shape

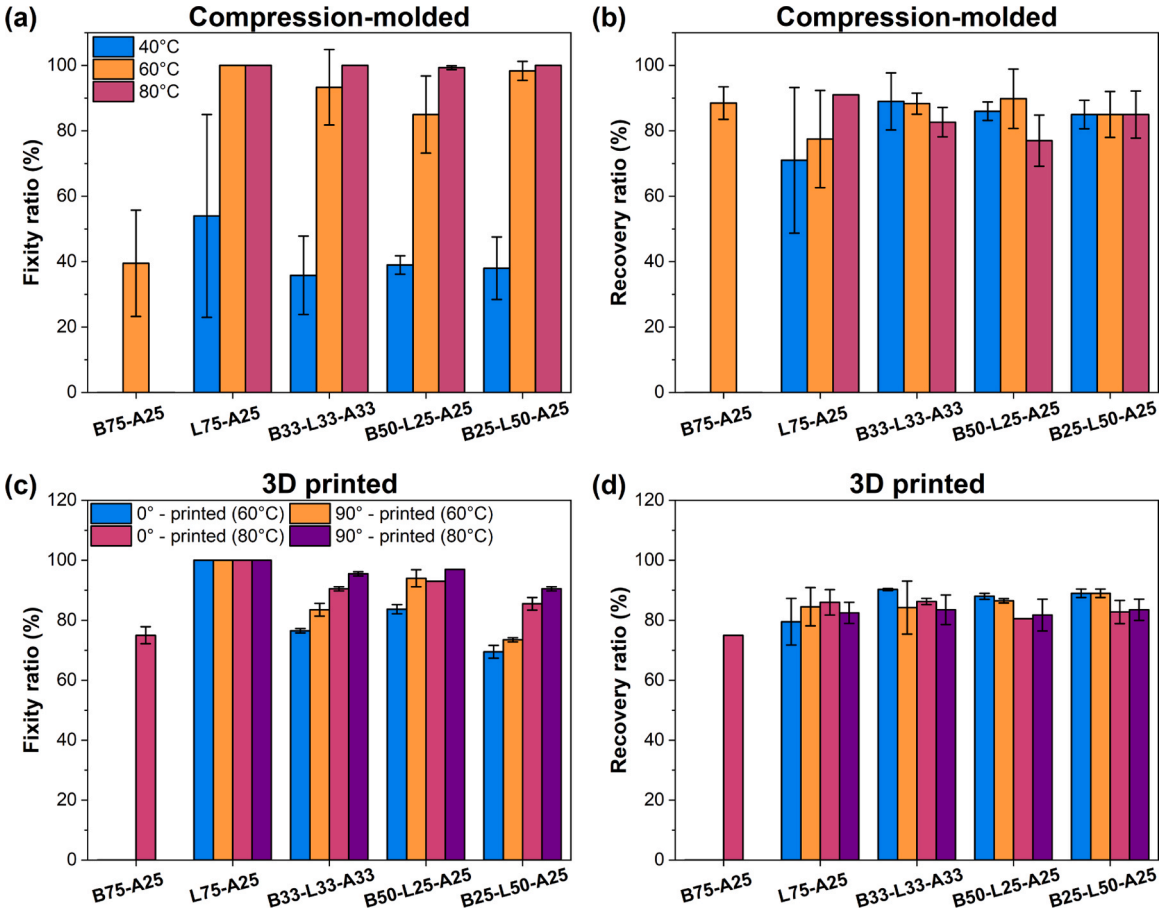

Fig. 8. Fixity and recovery ratios of (a, b) compression-molded and (c, d) 0°- and 90°-printed samples at various programming temperatures.

fixity and recovery ratios of the printed samples. R_f exhibits excellent repeatability for both 0° and 90° printing orientations. The 90°-printed specimens consistently achieve slightly higher R_f values than the 0°-printed ones; however, in both cases, the R_f values remain approximately 5.0–10.0% lower than those of the corresponding compression-molded samples (Fig. 8a and b). In contrast, R_r shows the opposite trend, gradually decreasing with increasing programming temperature. Orientation-related differences are minor, although 90°-printed samples tend to exhibit marginally higher fixity and lower recovery than their 0°-printed counterparts, likely due to anisotropic structural features and variations in stress transfer efficiency [20,21]. The observed increase in R_f and decrease in R_r with temperature reflect the growing contribution of irreversible plastic deformation in the rubbery state [67]. This balance highlights that high programming temperatures improve fixation but partially compromise recovery ability.

3.6.3. *Effect of SME cycles*

Fig. 9a shows the evolution of the fixation R_f and recovery R_r ratios for compression-molded samples of L75-A25, B25-L50-A25, and B33-L33-A33 as a function of the number of SME cycles. Blends B75-A25 and B50-L25-A25 were not included in the cyclic SME tests due to their brittleness and insufficient shape memory performance. Among the studied compositions, L75-A25 sheets exhibited the most stable performance, maintaining an excellent fixation ratio close to 100% even after 15 cycles. In contrast, B25-L50-A25 and B33-L33-A33 sheets showed lower fixation stability, with R_f gradually decreasing as the number of cycles increased. Recovery ratios R_r decreased progressively for all three blends, following a similar trend of deterioration with increasing cycle number. This decline can be attributed to stress-relaxation phenomena and structural failure, which, during repeated deformation and recovery cycles, lead to the gradual release of stored internal stresses, chain disentanglement, and the accumulation of microdamage [30]. As a result, the driving force for shape recovery diminishes over time [62,66,67]. B33-L33-A33 samples failed after 7 cycles, suggesting that this composition lacks sufficient network stability to withstand repeated programming and recovery.

These results demonstrate that L75-A25 sheets exhibit superior durability and cyclic stability of SME, whereas B25-L50-A25 and B33-L33-A33 suffer from progressive fatigue-induced degradation. These cyclic SME trends correlate well with the morphological features observed in SEM (Fig. 2). For example, B33-L33-A33 possess coarser, partially phase-separated structures that promote interfacial debonding and microvoid growth during repeated loading. Such morphological heterogeneity accelerates fatigue-induced damage and loss of SME function [67]. Overall, these results directly link the microstructure to the long-term performance of bio-based SMP blends.

Fig. 9b, c, d presents the evolution of the R_f and R_r of 3D printed L75-A25, B25-L50-A25, and B33-L33-A33 samples during cyclic SME testing. Printed samples demonstrated higher durability than compression-molded sheets, maintaining their functionality after 15 cycles without catastrophic failure. R_f of 3D-printed samples was generally lower than that of compression-molded sheets. In contrast, compression-molded blends exhibited more pronounced degradation of R_f (Fig. 9a). The R_r of 3D printed samples was consistently higher than that of the compression-molded sheets, confirming the improved reversibility of deformation in the printed structures. The layer-by-layer printed architecture may facilitate stress redistribution and mitigate the accumulation of localized damage that typically develops in bulk sheets [62,66,67]. This structural heterogeneity likely enhances resistance to crack initiation and propagation, allowing printed samples to sustain repeated

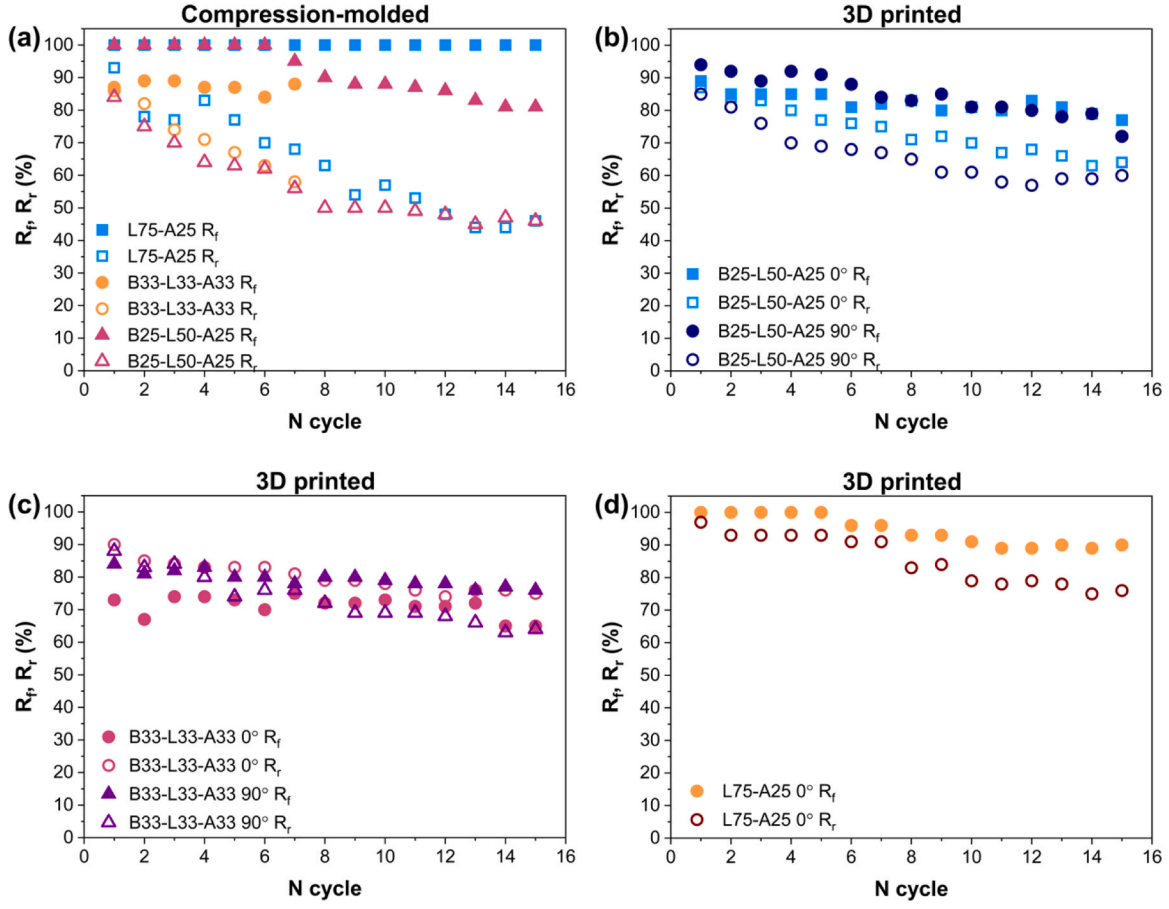

Fig. 9. Fixity (R_f) and recovery (R_r) ratios of (a) compression-molded and (b, c, d) 3D printed samples as functions of SME cycle number; T_p = 60 °C.

SME cycles without significant performance loss [5–7].

90°-printed samples exhibited slightly higher R_f values than 0°-printed samples. The anisotropic nature of the printed microstructure can explain this behavior. In 0°-printed samples, the molten strand paths are oriented along the thickness direction; therefore, during bending, the deformation is accommodated more uniformly within the continuous strands, which favors recovery. In contrast, in 90°-printed samples, the molten strands are oriented across the bending direction, which more strongly constrains deformation and thus enhances fixation. However, this same orientation amplifies stress concentrations at interlayer interfaces, thereby reducing the amount of recoverable elastic energy and lowering recovery efficiency [10].

3.6.4. *Effect of programming time*

Fig. 10 illustrates the effect of programming time on the SME behavior. The effect was investigated in the cold-programming regime using a L75-A25 compression-molded blend as a representative example, with the programming temperature set at 40 °C, corresponding to the onset of the glass-to-rubbery transition (Table 3, Fig. 4d). At higher programming temperatures, relaxation processes occur rapidly and fixation is almost instantaneous, making the study of time effects less relevant.

The R_f increases with fixation time, reflecting the progressive stress relaxation that allows the temporary shape to be more effectively locked in. This trend is cumulative, as successive cycles lead to further stabilization of R_f (Fig. 10 b), suggesting that prolonged relaxation promotes more efficient molecular rearrangement during fixation. In contrast, the R_r exhibits an opposite tendency, gradually decreasing with longer loading times and with increasing cycle number. Such opposing tendencies demonstrate the viscoelastic interplay between the stabilization of the temporary shape and the retention of recovery force [94]. However, when the programmed samples were subsequently heated above T_g (~70 °C), all samples, regardless of fixation time, recovered to the same R_r of approximately 80.0%, consistent with the earlier tests. This demonstrates that the time-dependent reduction in R_r observed at 40 °C is primarily associated with the viscoelastic response of the blends rather than irreversible viscoplastic deformation, and that recovery capacity is preserved as long as sufficient thermal mobility is provided [95]. The L75-A25 blend demonstrates the ability to be effectively programmed at relatively low or "cold" temperatures, offering clear advantages in reduced energy input and broader application potential.

3.7. *Discussion and Perspectives*

Currently, SMPs are mainly being developed for their unique functional performance. Their reversible deformation and diverse actuation mechanisms enable applications in biomedical devices, soft robotics, and 4D printing [9]. Bio-based SMPs are an emerging direction driven by biocompatibility [96], providing a promising platform for biomedical applications, as well as by sustainability goals aimed at reducing reliance on fossil resources and pollution [97].

Boonnao et al. [98] demonstrated that high-performance shape-memory behavior in 4D-printed polymers can be achieved by forming interpenetrating polymer networks via dual-curing processes. This approach resulted in near-complete shape fixity and recovery, as well as stable cyclic performance. However, such systems rely on relatively complex processing routes and thermoset-based chemistries. Rahmatabadi et al. [81] investigated the shape memory behavior of PLA/PBAT blends processed via Fused Deposition Modeling (FDM) 3D printing. They reported that increasing the PBAT content significantly reduces the recovery time, with shape recovery above 90% achieved in less than 2 s for blends containing 45 wt% PBAT. However, this improvement in recovery speed was accompanied by a slight decrease in the final recovery ratio. Rahmatabadi et al. focused primarily on composition-dependent recovery speed, the results here show that comparable or improved SME performance can be achieved through control of processing conditions, including anisotropy introduced during FGF printing and programming temperature. Hamidi et al. [99] investigated the shape memory behavior of PLA/thermoplastic polyurethane (TPU) blends fabricated via FDM 3D printing and reported that increasing TPU content reduced recovery to approximately 82–84% compared to PLA's R_r ≈ 97.0%. The authors showed that printing parameters significantly influence shape recovery, with layer thickness and raster angle contributing the most (36–40% and 35–39%, respectively). In contrast, the shape fixity ratio (R_f ≈ 95.0–99.0%) remained high and was largely insensitive to processing conditions. Song et al. [100] showed that compatibilization significantly improved shape fixity in PLA/ poly (caprolactone) PCL blends, increasing R_f from 55.0% to 93.0%, while maintaining high recovery (R_r ≈ 100%). This highlights the importance of interfacial compatibility between different polyesters. In the present study, PBSA exhibits good compatibility with PLA, which contributes to the high shape memory performance without the need for additional compatibilization.

The findings suggest that simple and sustainable material systems can provide competitive performance without relying on complex chemistries. In addition, the present work provides a systematic experimental dataset linking composition, processing route, and programming conditions.

4. Conclusion

Shape memory performance of PHB/PLA/PBSA blends depends on the combined effects of composition, processing route, and programming conditions. The overall etched phase morphology was similar for

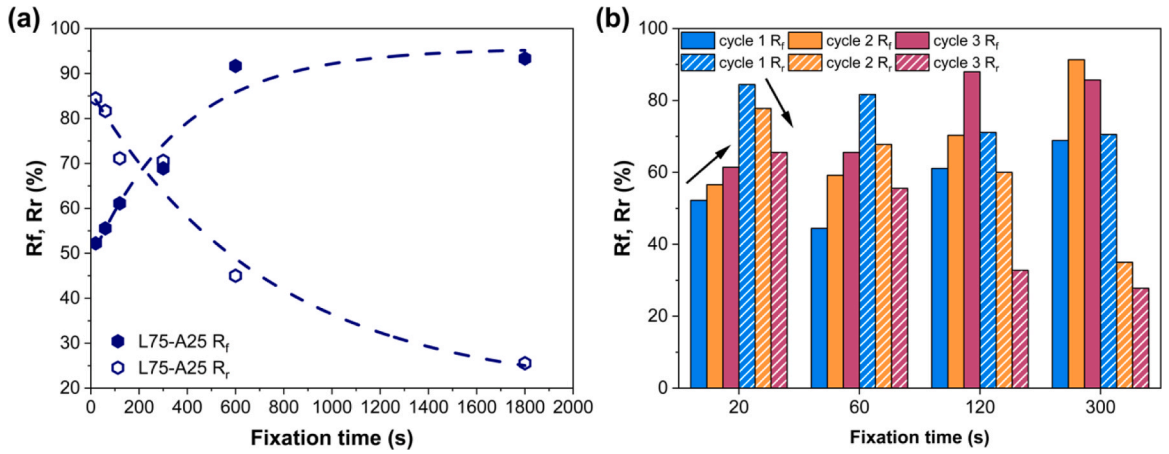

Fig. 10. (a) Fixity (R_f) and recovery (R_r) ratios of PLA75/PBSA25 compression-molded blend at various fixation times; (b) R_f and R_r in three SME cycles; T_p = 40 °C.

compression-molded and FGF-processed samples, but the printing process introduced orientation and structural anisotropy, which influenced the mechanical behavior and cyclic durability.

All blends exhibited non-Newtonian, shear-thinning behavior suitable for FGF 3D printing, with ternary systems showing improved elasticity and melt stability compared to binary formulations. Thermal and dynamic mechanical analysis results indicated that PLA-rich blends maintained higher stiffness and stronger phase coupling, while PHB contributed to broader relaxations. The tensile properties of the 3D printed samples were comparable to those of the compression-molded samples, suggesting that the FGF process can achieve similar mechanical performance.

Among the investigated compositions, the PLA-rich blend (L75-A25) showed the best balance between mechanical properties and shape memory performance. L75-A25 compression-molded samples exhibited $R_f = 100\%$ and $R_r = 89.0\%$, while 3D-printed samples (0°) showed similar fixity and higher recovery ($R_r = 79.5\%$). After 15 cycles, recovery decreased to $\approx 46.0\%$ for compression-molded samples and $\approx 76.0\%$ for 3D-printed samples, while fixity remained close to 100%. 90°-printed samples exhibited marginally higher fixity but lower recovery, confirming that anisotropy primarily affected mechanical load transfer rather than intrinsic SME response. Programming temperature is a key parameter: warm programming (60 °C) resulted in the most consistent performance, whereas cold (40 °C) and hot (80 °C) programming led to reduced fixity or recovery.

A strong correlation was established between stiffness, phase continuity, and shape memory efficiency. The results also suggest that shape memory behavior in these bio-based blends can be adjusted through processing and programming conditions without changing composition. This is relevant for the design of sustainable 4D-printed components, where both mechanical performance and functional response need to be controlled.

CRediT authorship contribution statement

Alisa Ponkratenkova: Writing – original draft, Visualization, Validation, Investigation, Formal analysis, Data curation. **Sergejs Beluns:** Writing – review & editing, Funding acquisition, Conceptualization. **Olesja Starkova:** Writing – review & editing, Writing – original draft, Visualization, Validation, Investigation, Formal analysis, Data curation, Conceptualization. **Anete Tropa:** Visualization, Investigation. **Oskars Platnieks:** Writing – review & editing, Writing – original draft, Validation, Formal analysis, Data curation. **Roland Kádár:** Writing – review & editing, Writing – original draft, Formal analysis. **Toms Valdemars Eiduks:** Investigation. **Sergejs Gaidukovs:** Writing – review & editing, Writing – original draft, Supervision, Resources, Methodology, Conceptualization.

Declaration of Competing Interest

The authors declare that they have no known competing financial interests or personal relationships that could have appeared to influence the work reported in this paper.

Acknowledgements

Alisa Ponkratenkova, Olesja Strakova, and Sergejs Beluns have been supported by grant No. RTU-ZG-2024/1–0029 under the EU Recovery and Resilience Facility funded project No. 5.2.1.1.i.0/2/24/I/CFLA/003 "Implementation of consolidation and management changes at Riga Technical University, Liepaja University, Rezekne Academy of Technology, Latvian Maritime Academy and Liepaja Maritime College for the progress towards excellence in higher education, science, and innovation". Alisa Ponkratenkova has been supported by the EU Recovery and Resilience Facility within the Project No 5.2.1.1.i.0/2/24/I/CFLA/003 “Implementation of consolidation and management changes at Riga Technical University, Liepaja University, Rezekne Academy of Technology, Latvian Maritime Academy and Liepaja Maritime College for the progress towards excellence in higher education, science and innovation” academic career doctoral grant (ID 1027).

Appendix A. Supporting information

Supplementary data associated with this article can be found in the online version at doi:10.1016/j.mtcomm.2026.115415.

Data availability

Data will be made available on request.

References

[1] C. Rathinasuriyan, J.B. Chandar, N. Lenin, M. Puviyarasan, Exploring materials, technologies, applications, and future outlooks in 4D printing: a comprehensive survey, Prog. Addit. Manuf. 10 (2025) 5883–5901, https://doi.org/10.1007/s40964-025-01034-3.

[2] D. Rahmatabadi, M.A. Yousefi, S. Shamsolhodaei, M. Baniassadi, K. Abrinia, M. Bodaghi, M. Baghani, 4D Printing of Polyethylene Glycol-Grafted Carbon Nanotube-Reinforced Polyvinyl Chloride–Polycaprolactone Composites for Enhanced Shape Recovery and Thermomechanical Performance, Adv. Intell. Syst. 7 (2025) 2500113, https://doi.org/10.1002/aisy.202500113.

[3] J. Li, Z. Liang, T. Li, Q. Wan, X. Huang, Q. Kan, A comprehensive review on 4D printing and applications of thermo-induced shape memory polymers, Int. J. Smart Nano Mater. 16 (2025) 24–83, https://doi.org/10.1080/19475411.2025.2458833.

[4] M.Y. Razzaq, J. Gonzalez-Gutierrez, G. Mertz, D. Ruch, D.F. Schmidt, S. Westermann, 4D Printing of Multicomponent Shape-Memory Polymer Formulations, Appl. Sci. 12 (2022) 7880, https://doi.org/10.3390/app12157880.

[5] S. Yan, F. Zhang, L. Luo, L. Wang, Y. Liu, J. Leng, Shape Memory Polymer Composites: 4D Printing, Smart Structures, and Applications, Research 6 (2023) 0234, https://doi.org/10.34133/research.0234.

[6] C. Zeng, L. Liu, W. Bian, Y. Liu, J. Leng, 4D printed electro-induced continuous carbon fiber reinforced shape memory polymer composites with excellent bending resistance, Compos. B Eng. 194 (2020) 108034, https://doi.org/10.1016/j.compositesb.2020.108034.

[7] H. Cui, S. Miao, T. Esworthy, S.J. Lee, X. Zhou, S.Y. Hann, T.J. Webster, B. T. Harris, L.G. Zhang, A novel near-infrared light responsive 4D printed nanoarchitecture with dynamically and remotely controllable transformation, Nano Res 12 (2019) 1381–1388, https://doi.org/10.1007/s12274-019-2340-9.

[8] M.A. Yousefi, D. Rahmatabadi, M. Baniassadi, M. Bodaghi, M. Baghani, 4D Printing of Multifunctional and Biodegradable PLA-PBAT-Fe3O4 Nanocomposites with Supreme Mechanical and Shape Memory Properties, Macromol. Rapid Commun. 46 (2025) 2400661, https://doi.org/10.1002/marc.202400661.

[9] K. Mirasadi, M.A. Yousefi, L. Jin, D. Rahmatabadi, M. Baniassadi, W.H. Liao, M. Bodaghi, M. Baghani, 4D Printing of Magnetically Responsive Shape Memory Polymers: Toward Sustainable Solutions in Soft Robotics, Wearables, and Biomedical Devices, Adv. Sci. 15 (2025) e13091, https://doi.org/10.1002/advs.202513091.

[10] K. Bouguermouh, M. Habibi, L. Laperrière, Z. Li, Y. Abdin, Designing advanced 4D printing thermo-sensitive shape memory polymer blends for enhanced mechanical and shape memory performances, Prog. Addit. Manuf. 10 (2025) 6507–6526, https://doi.org/10.1007/s40964-025-00989-7.

[11] C.P. Kumar, N. Sivanagaraju, M.R.K. Vakkalagadda, Shape memory polymers and composites in 4D printing: techniques and applications, Prog. Addit. Manuf. 10 (2025) 7263–7289, https://doi.org/10.1007/s40964-025-01099-0.

[12] M. López-Valdeolivas, D. Liu, D.J. Broer, C. Sánchez-Somolinos, 4D Printed Actuators with Soft-Robotic Functions, Macromol. Rapid Commun. 39 (2018) 1700710, https://doi.org/10.1002/marc.201700710.

[13] H.M. Pan, J. Sarkar, A. Goto, Networking of Block Copolymer Nano-assemblies via Digital Light Processing (DLP) 4D Printing for Programmable Actuation, ACS Appl. Polym. Mater. 4 (2022) 8676–8683, https://doi.org/10.1021/acsapm.2c01617.

[14] M.A. Yousefi, D. Rahmatabadi, M. Ahmadi, A. Bayati, M. Baniassadi, A. Laachachi, V.V. Silberschmidt, D. George, M. Baghani, 4D printing for minimally invasive biomedical applications: programmable smart materials for deployable devices, drug delivery, and tissue regeneration, Mater. Des. 263 (2026) 115555, https://doi.org/10.1016/j.matdes.2026.115555.

[15] M. Ramezani, Z.Mohd Ripin, 4D Printing in Biomedical Engineering: Advancements, Challenges, and Future Directions, J. Funct. Biomater. 14 (2023) 347, https://doi.org/10.3390/jfb14070347.

[16] R. Das, T.L. Cabaniss, S.A. Pineda-Castillo, B.N. Bohnstedt, Y. Liu, C.H. Lee, Design of thermally programmable 3D shape memory polymer-based devices tailored for endovascular treatment of intracranial aneurysms, J. Mech. Behav. Biomed. Mater. 160 (2024) 106784, https://doi.org/10.1016/j.jmbbm.2024.106784.

[17] T. van Manen, S. Janbaz, K.M.B. Jansen, A.A. Zadpoor, 4D printing of reconfigurable metamaterials and devices, Commun. Mater. 2 (2021) 56, https://doi.org/10.1038/s43246-021-00165-8.
[18] X. Zhou, L. Ren, Z. Song, G. Li, J. Zhang, B. Li, Q. Wu, W. Li, L. Ren, Q. Liu, Advances in 3D/4D printing of mechanical metamaterials: From manufacturing to applications, Compos. B Eng. 254 (2023) 110585, https://doi.org/10.1016/j.compositesb.2023.110585.
[19] F. Wenz, D. Schönfeld, S.C.L. Fischer, T. Pretsch, C. Eberl, Controlling Malleability of Metamaterials through Programmable Memory, Adv. Eng. Mater. 25 (2023) 2201022, https://doi.org/10.1002/adem.202201022.
[20] J. Zhao, M. Han, L. Li, Characterization of Anisotropic Shape Memory Behavior of Thermoresponsive Components in 4D Printing, 3D Print. Addit. Manuf. 11 (2024) 1055–1063, https://doi.org/10.1089/3dp.2023.0165.
[21] Á.S. Olalla, J.L. Cerezo, V.R. Abarca, L.R. Soriano, G. Mazzinari, E.G. Torres, Impact of Raster Angle on 3D Printing of Poly(Lactic Acid)/Thermoplastic Polyurethane Blends: Effects on Mechanical and Shape Memory Properties, Macromol. Mater. Eng. 310 (2025) 2400427, https://doi.org/10.1002/mame.202400427.
[22] K. Pieri, B.M. Felix, T. Zhang, P. Soman, J.H. Henderson, Printing Parameters of Fused Filament Fabrication Affect Key Properties of Four-Dimensional Printed Shape-Memory Polymers, 3D Print. Addit. Manuf. 10 (2023) 279–288, https://doi.org/10.1089/3dp.2021.0072.
[23] M. Kervran, C. Vagner, M. Cochez, M. Ponçot, M.R. Saeb, H. Vahabi, Thermal degradation of polylactic acid (PLA)/polyhydroxybutyrate (PHB) blends: A systematic review, Polym. Degrad. Stab. 201 (2022) 109995, https://doi.org/10.1016/j.polymdegradstab.2022.109995.
[24] X. Yang, H. Xu, K. Odelius, M. Hakkarainen, Poly(lactide)-g-poly(butylene succinate-co-adipate) with high crystallization capacity and migration resistance, Materials 9 (2016) 313, https://doi.org/10.3390/ma9050313.
[25] J. Mathew, J.P. Das, M. Tp, S. Kumar, Development of poly (butylene adipate-co-terephthalate) PBAT toughened poly (lactic acid) blends 3D printing filament, J. Polym. Res. 29 (2022) 474, https://doi.org/10.1007/s10965-022-03320-y.
[26] W. Kanabenja, K. Passarapark, T. Subchokpool, N. Nawaaukkaratharnant, A. J. Román, T.A. Osswald, C. Aumnate, P. Potiyaraj, 3D printing filaments from plasticized Polyhydroxybutyrate/Polylactic acid blends reinforced with hydroxyapatite, Addit. Manuf. 59 (2022) 103130, https://doi.org/10.1016/j.addma.2022.103130.
[27] A. Fallah, Q. Saleem, B. Koc, Assessment of mechanical properties and shape memory behavior of 4D printed continuous fiber-reinforced PETG composites, Compos. Part A Appl. Sci. Manuf. 181 (2024) 108165, https://doi.org/10.1016/j.compositesa.2024.108165.
[28] D. Rahmatabadi, K. Soltanmohammadi, M. Pahlavani, M. Aberoumand, E. Soleyman, I. Ghasemi, M. Baniassadi, K. Abrinia, M. Bodaghi, M. Baghani, Shape memory performance assessment of FDM 3D printed PLA-TPU composites by Box-Behnken response surface methodology, Int. J. Adv. Manuf. Technol. 127 (2023) 935–950, https://doi.org/10.1007/s00170-023-11571-2.
[29] D. Rahmatabadi, I. Ghasemi, M. Baniassadi, K. Abrinia, M. Baghani, 4D printing of PLA-TPU blends: effect of PLA concentration, loading mode, and programming temperature on the shape memory effect, J. Mater. Sci. 58 (2023) 7227–7243, https://doi.org/10.1007/s10853-023-08460-0.
[30] C. Schmidt, K. Neuking, G. Eggeler, Functional fatigue of Shape memory polymers, Adv. Eng. Mater. 10 (2008) 922–927, https://doi.org/10.1002/adem.200800213.
[31] A. Lendlein, O.E.C. Gould, Reprogrammable recovery and actuation behaviour of shape-memory polymers, Nat. Rev. Mater. 4 (2019) 116–133, https://doi.org/10.1038/s41578-018-0078-8.
[32] Z. Wang, J. Liu, J. Guo, X. Sun, L. Xu, The study of thermal, mechanical and shape memory properties of chopped carbon fiber-reinforced TPI shape memory polymer composites, Polymers 9 (2017) 594, https://doi.org/10.3390/polym9110594.
[33] M. Aberoumand, D. Rahmatabadi, K. Soltanmohammadi, E. Soleyman, I. Ghasemi, M. Baniassadi, K. Abrinia, M. Bodaghi, M. Baghani, Stress recovery and stress relaxation behaviors of PVC 4D printed by FDM technology for high-performance actuation applications, Sens. Actuators A Phys. 361 (2023) 114572, https://doi.org/10.1016/j.sna.2023.114572.
[34] A. Kallel, A.B. Abdallah, F. Gamaoun, S. Farzaneh, H. BenDaly, J. Fitoussi, A. Tcharkhtchi, Driving force for shape memory effect of polymers, J. Polym. Res. 28 (2021) 308, https://doi.org/10.1007/s10965-021-02637-4.
[35] M. Barbier, M.J. Le Guen, J. McDonald-Wharry, J.H. Bridson, K.L. Pickering, Quantifying the Shape Memory Performance of a Three-Dimensional-Printed Biobased Polyester/Cellulose Composite Material, 3D Print. Addit. Manuf. 8 (2021) 193–200, https://doi.org/10.1089/3dp.2020.0166.
[36] E. Soleyman, D. Rahmatabadi, K. Soltanmohammadi, M. Aberoumand, I. Ghasemi, K. Abrinia, M. Baniassadi, K. Wang, M. Baghani, Shape memory performance of PETG 4D printed parts under compression in cold, warm, and hot programming, Smart Mater. Struct. 31 (2022) 085002, https://doi.org/10.1088/1361-665X/ac77cb.
[37] S.R. Merouani, R. Kulagin, V. Bondarenko, R. Hosseinnezhad, F. Zaïri, I. Vozniak, Strategy for Fabricating Multiple-Shape Memory Polymeric Materials Based on Solid State Mixing, ACS Macro Lett. 14 (2025) 129–134, https://doi.org/10.1021/acsmacrolett.4c00601.
[38] M. Anthamatten, K. Cavicchi, G. Li, A. Wang, Cold, warm, and hot programming of shape memory polymers, J. Polym. Sci. B Polym. Phys. 54 (2016) 1319–1339, https://doi.org/10.1002/polb.24041.
[39] K. Shahi, R. Boomurugan, R. Velmurugan, Cold programming of epoxy-based shape memory polymer, Structures 29 (2021) 2082–2093, https://doi.org/10.1016/j.istruc.2020.05.023.
[40] K. Shahi, V. Ramachandran, Theoretical and Experimental Investigation of Shape Memory Polymers Programmed below Glass Transition Temperature, Polymers 14 (2022) 2753, https://doi.org/10.3390/polym14132753.
[41] A. Curmi, A. Rochman, Screw extrusion fused granulate Fabrication: Trends, materials, extruder classification and future development, Polymer 330 (2025) 128459, https://doi.org/10.1016/j.polymer.2025.128459.
[42] M. Yousfi, A. Belhadj, K. Lamnawar, A. Maazouz, 3D printing of PLA and PMMA multilayered model polymers: an innovative approach for a better-controlled pellet multi-extrusion process, ESAFORM Fr. (2021), https://doi.org/10.25518/esaform21.1024.
[43] H. Liu, K. Gong, A. Portela, Z. Cao, R. Dunbar, Y. Chen, Granule-based material extrusion is comparable to filament-based material extrusion in terms of mechanical performances of printed PLA parts: A comprehensive investigation, Addit. Manuf. 75 (2023) 103744, https://doi.org/10.1016/j.addma.2023.103744.
[44] A. Curmi, A. Rochman, Miniaturized fused granulate fabrication of polyether ether ketone (PEEK, Prog. Addit. Manuf. 9 (2024) 1265–1275, https://doi.org/10.1007/s40964-023-00518-4.
[45] B. Huang, E. Aslan, Z. Jiang, E. Daskalakis, M. Jiao, A. Aldalbahi, C. Vyas, P. Bártolo, Engineered dual-scale poly (ε-caprolactone) scaffolds using 3D printing and rotational electrospinning for bone tissue regeneration, Addit. Manuf. 36 (2020) 101452, https://doi.org/10.1016/j.addma.2020.101452.
[46] D. Moreno Nieto, V. Casal López, S.I. Molina, Large-format polymeric pellet-based additive manufacturing for the naval industry, Addit. Manuf. 23 (2018) 79–85, https://doi.org/10.1016/j.addma.2018.07.012.
[47] W. Yu, Z. Hu, Y. Zhang, Y. Zhang, W. Dong, X. Li, S. Wang, Compatibilizing Biodegradable Poly(lactic acid)/polybutylene adipate-co-terephthalate Blends via Reactive Graphene Oxide for Screw-Based 3D Printing, Polymers 15 (2023) 3992, https://doi.org/10.3390/polym15193992.
[48] D. Rigon, F. Florian, M. Ricotta, G. Ardengo, F. Trivillin, G. Meneghetti, Fatigue behaviour of 3D printed virgin and recycled short-glass-fiber-reinforced and mineral-filled polypropylene, in: Procedia Structural Integrity, Elsevier B.V, 2021, pp. 199–204, https://doi.org/10.1016/j.prostr.2021.12.029.
[49] O. Platnieks, A. Ponkratenkova, M. Nabels-Sneiders, D. Veidmanis, K. Smits, V. K. Thakur, S. Gaidukovs, High wood content / Poly(Butylene succinate) composites 3D-printed by fused granulate fabrication, Polym. Test. 156 (2026) 109121, https://doi.org/10.1016/j.polymertesting.2026.109121.
[50] L. Fontana, A. Giubilini, R. Arrigo, G. Malucelli, P. Minetola, Characterization of 3D Printed Polylactic Acid by Fused Granular Fabrication through Printing Accuracy, Porosity, Thermal and Mechanical Analyses, Polymers 14 (2022) 3530, https://doi.org/10.3390/polym14173530.
[51] B.V. Reddy, N.V. Reddy, A. Ghosh, Fused deposition modelling using direct extrusion, Virtual Phys. Prototyp. 2 (2007) 51–60, https://doi.org/10.1080/17452750701336486.
[52] A. Bayati, M.A. Yousefi, D. Rahmatabadi, M. Baniassadi, K. Abrinia, M. Bodaghi, D. George, M. Baghani, 3D printing thermoplastic vulcanizates: Current limitations, innovative solutions, and emerging applications, Mater. Today Adv. 28 (2025) 100664, https://doi.org/10.1016/j.mtadv.2025.100664.
[53] E. Meraz Trejo, X. Jimenez, K.M.M. Billah, J. Seppala, R. Wicker, D. Espalin, Compressive deformation analysis of large area pellet-fed material extrusion 3D printed parts in relation to in situ thermal imaging, Addit. Manuf. 33 (2020) 101099, https://doi.org/10.1016/j.addma.2020.101099.
[54] T. Cersoli, A. Cresanto, C. Herberger, E. Macdonald, P. Cortes, 3d printed shape memory polymers produced via direct pellet extrusion, Micromachines 12 (2021) 1–12, https://doi.org/10.3390/mi12010087.
[55] A. Sabalina, S. Gaidukovs, M. Jurinovs, L. Grase, O. Platnieks, Fabrication of poly (lactic acid), poly(butylene succinate), and poly(hydroxybutyrate) bio-based and biodegradable blends for application in fused filament fabrication-based 3D printing, J. Appl. Polym. Sci. 140 (2023) 501–512, https://doi.org/10.1002/app.54031.
[56] A. Sabalina, O. Platnieks, G. Gaidukova, A. Aunins, T.V. Eiduks, S. Gaidukovs, Thermomechanical and mechanical analysis of polylactic acid/polyhydroxyalkanoate/poly(butylene succinate-co-adipate) binary and ternary blends, RSC Adv. 15 (2025) 501–512, https://doi.org/10.1039/d4ra05684a.
[57] A. Sabalina, S. Gaidukovs, A. Aunins, A. Gromova, G. Gaidukova, L. Orlova, O. Platnieks, Exploring the Processing Potential of Polylactic Acid, Polyhydroxyalkanoate, and Poly(butylene succinate-co-adipate) Binary and Ternary Blends, Polymers 16 (2024) 2288, https://doi.org/10.3390/polym16162288.
[58] A. Sabalina, S. Gaidukovs, O. Platnieks, O. Starkova, G. Gaidukova, L. Orlova, M. Jurinovs, Environmental degradation and durability of bulk 3D-printed parts from biodegradable polyester blends of PBS, PLA, and PHB in seawater, RSC Sustain. 3 (2025) 4049–4066, https://doi.org/10.1039/d5su00275c.
[59] Z. Yu, Z. Wang, H. Li, J. Teng, L. Xu, Shape memory epoxy polymer (SMEP) composite mechanical properties enhanced by introducing graphene oxide (GO) into the matrix, Materials 12 (2019) 1107, https://doi.org/10.3390/ma12071107.
[60] L.A. Pinto, E.H. Backes, S.V. Harb, G.M. Pinto, D.A.L.V. da Cunha, R.J.E. Andrade, G.J.M. Fechine, H.S. Selistre-de-Araújo, L.C. Costa, L.A. Pessan, Shape memory thermoplastic polyurethane/polycaprolactone blend and composite with hydroxyapatite for biomedical application, J. Mater. Res. 39 (2024) 90–106, https://doi.org/10.1557/s43578-023-01172-w.

[61] D. Lascano, L. Quiles-Carrillo, R. Balart, T. Boronat, N. Montanes, Toughened poly (lactic acid)-PLA formulations by binary blends with poly(butylene succinate-co-adipate)-PBSA and their shape memory behaviour, Materials 12 (2019) 622, https://doi.org/10.3390/ma12040622.
[62] R. Sanaka, S.K. Sahu, P.S.R. Sreekanth, J. Giri, F. Mohammad, H.A. Al-Lohedan, M.S. Saharudin, Q. Ma, Heat-Responsive PLA/PU/MXene Shape Memory Polymer Blend Nanocomposite: Mechanical, Thermal, and Shape Memory Properties, Polymers 17 (2025) 338, https://doi.org/10.3390/polym17030338.
[63] L. Mao, Q. Meng, A. Ahmad, Z. Wei, Mechanical analyses and structural design requirements for flexible energy storage devices, Adv. Energy Mater. 7 (2017) 1700535, https://doi.org/10.1002/aenm.201700535.
[64] N. Deka, A. Bera, D. Roy, P. De, Methyl Methacrylate-Based Copolymers: Recent Developments in the Areas of Transparent and Stretchable Active Matrices, ACS Omega 7 (2022) 36929–36944, https://doi.org/10.1021/acsomega.2c04564.
[65] M. Alsaadi, T.A. Sebaey, E.P. Hinchy, C.T. McCarthy, T.A. de, M. de Lima, A. Portela, D.M. Devine, Viscoelastic, Shape Memory, and Fracture Characteristics of 3D Printed Photosensitive Epoxy-Based Resin Under the Effect of Hydrothermal Ageing, J. Manuf. Mater. Process 9 (2025) 46, https://doi.org/10.3390/jmmp9020046.
[66] J. Zhao, M. Han, L. Li, Modeling and characterization of shape memory properties and decays for 4D printed parts using stereolithography, Mater. Des. 203 (2021) 109617, https://doi.org/10.1016/j.matdes.2021.109617.
[67] K. Bouguermouh, M. Habibi, L. Laperrière, Z. Li, Y. Abdin, 4D-printed PLA-PETG polymer blends: comprehensive analysis of thermal, mechanical, and shape memory performances, J. Mater. Sci. 59 (2024) 11596–11613, https://doi.org/10.1007/s10853-024-09862-4.
[68] R.B. da Cunha, P. Agrawal, A. da Silva Lúcio, C.T.C. Cunha, G. de Figueiredo Brito, T.J.A. de Mélo, Evaluation of shape memory and self-healing of poly (ε-caprolactone)/poly(ethylene-co-methacrylic acid) ionomer (PCL/EMAA-Zn) blends, J. Mater. Sci. 59 (2024) 4700–4721, https://doi.org/10.1007/s10853-024-09499-3.
[69] X. Huang, M. Panahi-Sarmad, K. Dong, R. Li, T. Chen, X. Xiao, Tracing evolutions in electro-activated shape memory polymer composites with 4D printing strategies: A systematic review, Compos. Part A Appl. Sci. Manuf. 147 (2021) 106444, https://doi.org/10.1016/j.compositesa.2021.106444.
[70] N.E. Zander, M. Gillan, Z. Burckhard, F. Gardea, Recycled polypropylene blends as novel 3D printing materials, Addit. Manuf. 25 (2019) 122–130, https://doi.org/10.1016/j.addma.2018.11.009.
[71] M. Ghelichi, N. Taheri Qazvini, S.H. Jafari, H.A. Khonakdar, U. Reuter, Nanoclay dispersion in a miscible blend: An assessment through rheological analysis, J. Polym. Res. 19 (2012) 9830, https://doi.org/10.1007/s10965-012-9830-8.
[72] J.D. Ferry, Viscoelastic Properties of Polymers, John Wiley & Sons, New York, 1980.
[73] M. Qahtani, F. Wu, M. Misra, S. Gregori, D.F. Mielewski, A.K. Mohanty, Experimental Design of Sustainable 3D-Printed Poly(Lactic Acid)/Biobased Poly (Butylene Succinate) Blends via Fused Deposition Modeling, ACS Sustain. Chem. Eng. 7 (2019) 14460–14470, https://doi.org/10.1021/acssuschemeng.9b01830.
[74] S. Weinmann, C. Bonten, Thermal and rheological properties of modified polyhydroxybutyrate (PHB, Polym. Eng. Sci. 59 (2019) 1057–1064, https://doi.org/10.1002/pen.25075.
[75] J.D. Conrad, G.M. HarrisonThe Rheology and Processing of Renewable Resource Polymers. AIP Conf. Proc. 1027 (2008) 114–116.
[76] D. Acierno, A. Patti, Fused Deposition Modelling (FDM) of Thermoplastic-Based Filaments: Process and Rheological Properties – An Overview, Materials 16 (2023) 7664, https://doi.org/10.3390/ma16247664.
[77] A. Patti, S. Acierno, G. Cicala, D. Acierno, Predicting the Printability of Poly (Lactide) Acid Filaments in Fused Deposition Modeling (FDM) Technology: Rheological Measurements and Experimental Evidence, ChemEngineering 7 (2023) 1, https://doi.org/10.3390/chemengineering7010001.
[78] M. Elbadawi, Polymeric Additive Manufacturing: The Necessity and Utility of Rheology, in: Polymer Rheology, InTech, 2018, https://doi.org/10.5772/intechopen.77074.
[79] Y. Zare, S.P. Park, K.Y. Rhee, Analysis of complex viscosity and shear thinning behavior in poly (lactic acid)/poly (ethylene oxide)/carbon nanotubes biosensor based on Carreau–Yasuda model, Results Phys. 13 (2019) 102245, https://doi.org/10.1016/j.rinp.2019.102245.
[80] J.W. Jang, K.E. Min, C. Kim, C. Wern, S. Yi, Rheological Properties and 3D Printing Behavior of PCL and DMSO2 Composites for Bio-Scaffold, Materials 17 (2024) 2459, https://doi.org/10.3390/ma17102459.
[81] D. Rahmatabadi, M. Khajepour, A. Bayati, K. Mirasadi, M. Amin Yousefi, A. Shegeft, I. Ghasemi, M. Baniassadi, K. Abrinia, M. Bodaghi, M. Baghani, Advancing sustainable shape memory polymers through 4D printing of polylactic acid-polybutylene adipate terephthalate blends, Eur. Polym. J. 216 (2024) 113289, https://doi.org/10.1016/j.eurpolymj.2024.113289.
[82] K. Szuman, I. Krucińska, M. Boguń, Z. Draczyński, PLA/PHA- biodegradable blends for pneumothermic fabrication of nonwovens, Autex Res. J. 16 (2016) 119–127, https://doi.org/10.1515/aut-2015-0047.
[83] BioPBS™ (bio-based polybutylene succinate) (2025). ⟨https://www.mcpp-global.com/en/mcpp-europe/products/brand/biopbsTM/⟩. Accessed 24 November 2025.
[84] Y. Kong, J.N. Hay, Multiple melting behaviour of poly(ethylene terephthalate, Polymer 3 (2003) 623–633, https://doi.org/10.1016/S0032-3861(02)00814-5.
[85] S.S. Ray, J. Bandyopadhyay, M. Bousmina, Thermal and thermomechanical properties of poly[(butylene succinate)-co-adipate] nanocomposite, Polym. Degrad. Stab. 92 (2007) 802–812, https://doi.org/10.1016/j.polymdegradstab.2007.02.002.
[86] S.Y. Hobbs, C.F. Pratt, Multiple melting in poly(butylene terephthalate, Polymer 16 (1975) 462–464, https://doi.org/10.1016/0032-3861(75)90258-X.
[87] G.W.H. Höhne, Another approach to the Gibbs-Thomson equation and the melting point of polymers and oligomers, Polymer 43 (2002) 4689–4698, https://doi.org/10.1016/S0032-3861(02)00305-1.
[88] R. Zhang, F. Du, K. Jariyavidyanont, E. Zhuravlev, C. Schick, R. Androsch, Glass transition temperature of poly(D,L-lactic acid) of different molar mass, Thermochim. Acta 718 (2022) 179387, https://doi.org/10.1016/j.tca.2022.179387.
[89] S. Zhou, A.N. Hrymak, M.R. Kamal, Properties of microinjection-molded multi-walled carbon nanotubes-filled poly(lactic acid)/poly[(butylene succinate)-co-adipate] blend nanocomposites, J. Mater. Sci. 53 (2018) 9013–9025, https://doi.org/10.1007/s10853-018-2193-8.
[90] H. Tsuji, M. Sawada, L. Bouapao, Biodegradable polyesters as crystallization-accelerating agents of poly(l -lactide), ACS Appl. Mater. Interfaces 1 (2009) 1719–1730, https://doi.org/10.1021/am9002759.
[91] L. Jiang, M.P. Wolcott, J. Zhang, Study of biodegradable polylactide/poly (butylene adipate-co-terephthalate) blends, Biomacromolecules 7 (2006) 199–207, https://doi.org/10.1021/bm050581q.
[92] S. Gopinath, N.N. Adarsh, P. Radhakrishnan Nair, S. Mathew, One-way thermo-responsive shape memory polymer nanocomposite derived from polycaprolactone and polystyrene-block-polybutadiene-block-polystyrene packed with carbon nanofiber, Mater. Today Commun. 22 (2020) 100802, https://doi.org/10.1016/j.mtcomm.2019.100802.
[93] E. Tekay, S. Şen, M.A. Korkmaz, N. Nugay, Preparation and characterization of thermo-responsive shape memory ester-based polymer blends, J. Mater. Sci. 58 (2023) 8241–8260, https://doi.org/10.1007/s10853-023-08549-6.
[94] M. Anthamatten, K. Cavicchi, G. Li, A. Wang, Cold, warm, and hot programming of shape memory polymers, J. Polym. Sci. B Polym. Phys. 54 (2016) 1319–1339, https://doi.org/10.1002/polb.24041.
[95] K. Shahi, R. Boomurugan, R. Velmurugan, Cold programming of epoxy-based shape memory polymer, Structures 29 (2021) 2082–2093, https://doi.org/10.1016/j.istruc.2020.05.023.
[96] Y. Guo, Z. Lv, Y. Huo, L. Sun, S. Chen, Z. Liu, C. He, X. Bi, X. Fan, Z. You, A biodegradable functional water-responsive shape memory polymer for biomedical applications, J. Mater. Chem. B 7 (2019) 123–132, https://doi.org/10.1039/c8tb02462f.
[97] N.A. Asri, N.A.A. Sezali, H.L. Ong, M.H. Mohd Pisal, Y.H. Lim, J. Fang, Review on Biodegradable Aliphatic Polyesters: Development and Challenges, Macromol. Rapid Commun. 45 (2024) 2400475, https://doi.org/10.1002/marc.202400475.
[98] N. Boonnao, P. Luengrojanakul, R. Gholami, C.H. Ahn, P. Karagiannidis, S. Rimdusit, High-performance 4D printing of shape memory polymers with interpenetrating networks from hybrid biobased benzoxazine with acrylic resin blends, Appl. Mater. Today 44 (2025) 102774, https://doi.org/10.1016/j.apmt.2025.102774.
[99] M.N. Hamidi, J. Abdullah, A.S. Mahmud, H. Namazi, Effect of blend ratios and printing parameters on PLA/TPU shape memory polymer performance, Polym. Test. 157 (2026) 109157, https://doi.org/10.1016/j.polymertesting.2026.109157.
[100] M. Song, S. Li, G. Zhu, J. Guo, Compatibilised and toughened of PLA/PCL blends via modified-chitosan linking amorphous regions: 4D printing and shape memory processes, Polym. Test. 125 (2023) 108105, https://doi.org/10.1016/j.polymertesting.2023.108105.